Title
De novo design of a transmembrane Zn^{2+}-transporting four-helix bundle.

Journal
Science (New York, N.Y.), 346(6216)

ISSN
0036-8075

Authors
Joh, Nathan H
Wang, Tuo
Bhate, Manasi P
et al.

Publication Date
2014-12-01

DOI
10.1126/science.1261172

Peer reviewed

PROTEIN DESIGN

De novo design of a transmembrane Zn^{2+}-transporting four-helix bundle

Nathan H. Joh,[1] Tuo Wang,[2] Manasi P. Bhate,[1] Rudresh Acharya,[3] Yibing Wu,[1] Michael Grabe,[1*] Mei Hong,[2*] Gevorg Grigoryan,[4*] William F. DeGrado[1*]

The design of functional membrane proteins from first principles represents a grand challenge in chemistry and structural biology. Here, we report the design of a membrane-spanning, four-helical bundle that transports first-row transition metal ions Zn^{2+} and Co^{2+}, but not Ca^{2+}, across membranes. The conduction path was designed to contain two di-metal binding sites that bind with negative cooperativity. X-ray crystallography and solid-state and solution nuclear magnetic resonance indicate that the overall helical bundle is formed from two tightly interacting pairs of helices, which form individual domains that interact weakly along a more dynamic interface. Vesicle flux experiments show that as Zn^{2+} ions diffuse down their concentration gradients, protons are antiported. These experiments illustrate the feasibility of designing membrane proteins with predefined structural and dynamic properties.

The de novo design of proteins is an important endeavor that critically tests our understanding of the principles underlying protein folding and function, while also laying the foundation for the design of proteins and molecular assemblies with desired properties. Much progress has been recently demonstrated in the design of water-soluble proteins with a variety of folds (*1*), and numerous natural proteins have been redesigned to bind metal ions (*2*) or small molecules (*3*) or to catalyze mechanistically simple reactions (*4*–*7*). However, the design of membrane proteins remains in its infancy (*8*, *9*). To date, the most complex designed membrane proteins contain porphyrins that catalyze transmembrane electron transfer (*8*), but no designed membrane protein has been experimentally shown to adopt the desired fold at atomic resolution.

Here, we focus on the design of a Zn^{2+} transporter, a goal that presents several challenges. First is to design a membrane protein with a predefined structure and, second, to determine its structure and dynamics at high resolution. Next, the design must precisely position polar ionizable Zn^{2+} ligands, which are ordinarily excluded from a membrane environment. Furthermore, proton-Zn^{2+} antiport requires thermodynamic coupling to link proton binding to changes in metal ion affinity. Finally, we aimed to anticipate and orchestrate dynamics to facilitate ion transport.

Here, we describe a computational strategy for the design of a Zn^{2+} transporter, dubbed Rocker, to characterize its structure, and demonstrate that it transports Zn^{2+} with concomitant reverse transport of protons. This work demonstrates the feasibility of membrane protein design and suggests that the advances recently reported in the design of water-soluble proteins can now be extended to membrane-spanning structures.

Natural transporters are hypothesized to rock between two or more states in a mechanism known as alternating access (*10*–*12*). For example, the multidrug transporter EmrE is a homodimer that is not stable in a single symmetric homodimeric conformation (*13*). Instead, it rocks between two degenerate asymmetric structures that alternately expose a substrate-binding site to the cytoplasmic and periplasmic sides of the membrane. Many transporters also harness the energy released in the movement of one ion down its concentration gradient to drive the accumulation of a second ion or small molecule. In proton-dependent transporters, protons often compete directly with substrates for binding to ionizable side chains. We sought to design a minimal protein that uses a similar mechanism. Four-helix bundles are capable of transporting protons (*14*–*16*) and binding metal ions, so we focused on this fold. Moreover, we previously observed that the Glu side chains in a 4Glu-2His di-Zn^{2+}–binding protein were largely protonated, even at neutral pH, in the absence of Zn^{2+}, because of the energetic cost of burying negatively charged side chains within the interior of a protein (*17*). Binding of Zn^{2+} displaces these protons, providing a means to achieve the desired thermodynamic coupling. Moreover, di-metal sites often have bridging water or hydroxide ligands, which could provide kinetically accessible sites for passing protons to the protein ligands as they diffuse through the channel.

We focused on design of a four-helix bundle with the helices inclined by a 10° to 20° angle (Fig. 1, A to D, and fig. S1); if the helices are straight, they diverge from a point of closest approach to yield a truncated conical shape. However, if they gently curve (as in a coiled-coil), the bundle has a more cylindrical shape. An appropriately designed antiparallel homotetramer might alternate between the two energetically equivalent asymmetric conformations with the wider end at one or the other side of the bundle. The highly symmetric coiled-coil might provide an intermediate state, facilitating movement of ions through the bundle (Fig. 1A). However, the coiled-coil should not be so stable as to kinetically trap the mobile ions. Thus, the process reduces to the design of an energy landscape in which the two degenerate asymmetric states are more stable than the symmetric coiled-coil.

We chose a homotetrameric bundle with two 2His4Glu di-Zn^{2+}–binding sites, each site formed by the coalescence of an EXXH motif near the N terminus of two helices and a Glu near the C terminus of the other two helices (Fig. 1, A and B). The symmetric coiled-coil was designed via a stochastic search in the space of Crick parameters (*18*, *19*) to find a backbone conformation that allowed Zn^{2+} binding in a good geometry (*20*, *21*). Moreover, we assured that the helix-helix interfaces would be "designable"; i.e., their backbone geometries should be well represented in a diverse set of native proteins (see fig. S1, E and F, and supplementary methods) (*19*). The resulting 25-residue-long antiparallel homotetrameric bundle shares no structural similarities with YiiP, the only natural Zn^{2+} transporter with a high-resolution structure (*22*). YiiP is a hexamer with a single 1His3Asp Zn^{2+} site.

We next created the off-symmetry version of the bundle by straightening helices beyond the boundaries of one metal-binding site, which caused subtle flaring of the bundle (up to 1.7 Å) and distorted the binding site at the opposite end of the oligomer (Fig. 1A). To stabilize this conformation relative to the symmetric coiled-coil, we used a negative design algorithm (*23*). This was a difficult task, given the high similarity between the structures. Negative design relies in part on introducing interactions to destabilize the symmetric conformation. If the backbone relaxes even subtly in an unanticipated manner, these interactions may become much less destabilizing. Moreover, conformational entropy may be significant for encoding preference for the asymmetric state. To address these issues, we defined configuration-space volume elements around the symmetric and asymmetric structures, and we used VALOCIDY (*24*) to estimate the free energy in each for the top ~1000 sequences predicted to be asymmetry-selective by initial negative design (NVT ensemble, IMM1 force field) (*25*). The final sequence chosen (Fig. 1C) was the one displaying the largest VALOCIDY-estimated free-energy difference between the two states, while having a sufficiently large pore to permit ion conduction. Residues allowed in design were defined, based on membrane depth using the E_Z potential (table S1) (*26*, *27*). We also required a second-shell H-bond to the metal binding His (*28*) (see supplementary methods for details).

[1]Department of Pharmaceutical Chemistry, Cardiovascular Research Institute, University of California, San Francisco, San Francisco, CA 94158, USA. [2]Department of Chemistry, Massachusetts Institute of Technology, Cambridge, MA 02139, USA. [3]School of Biological Sciences, National Institute of Science Education and Research, Bhubaneswar, Odisha, India. [4]Department of Computer Science and Department of Biological Sciences, Dartmouth College, Hanover, NH 03755, USA.
*Corresponding author. E-mail: william.degrado@ucsf.edu (W.F.D.); gevorg.grigoryan@dartmouth.edu (G.G.); meihong@mit.edu (M.H.); michael.grabe@ucsf.edu (M.G.)

The resulting dimer of dimers has two nonequivalent helix-helix interfaces (Fig. 1D); a "tight interface" has a small interhelical distance (8.9 Å) stabilized by efficient packing of small, Ala residues. The geometry of the tight interface is similar to the "alanine coil," a sequence-structure motif shown to impart thermodynamic stability and structural rigidity in model peptides (*29*). The "loose interface" has a larger interhelical distance of 12.0 Å packed by large Phe residues. The packing of large apolar residues in membrane proteins provides a much smaller driving force for association than the tight packing of small residues (*29*–*31*). Thus, we expected the loose interface to be thermodynamically less stable and geometrically more flexible, which would facilitate the motion of ions through the bundle.

Molecular dynamics (MD) simulations were used to probe the stability and dynamics of the de novo designed structure. We embedded the model structure in a homogenous 1-palmitoyl-2-oleoylphosphatidylcholine bilayer with two Zn^{2+} fully occupying one of the 4Glu-2His sites; the other site was empty as described in the supplement. The fully bound site is electrically neutral when the coordinating residues are in their standard protonation states (charged Glu and neutral His). To explore the role of protonation at the unliganded site, we carried out four independent simulations exploring different possible charge states (fig. S2, A to C). Qualitatively, all four simulations behave similarly on the 100-ns time scale. The chelated di-zinc site is extremely stable and shows a Cα root mean square deviation (RMSD) of about 0.75 Å with very few fluctuations (fig. S2A, right). Water enters the transporter, providing hydration by 10 to 14 water molecules along the lumen between the two binding sites, a desirable feature for ion transport (fig. S2E). Analogous to a hydrophobic gate, bulky aromatic Phe14 adjacent to the Zn^{2+} site appears to partially exclude water.

Next, we examined the distance between the helices in the tight versus loose dimer interfaces. The helices in the tight dimer remain closely packed near the initial structure (red curves, Fig. 1E and fig. S2B). However, the distance between helices in the weak interface increases by as much as 3 Å in three of four simulations (fig. S2B). The separation in the weak dimer interface is most pronounced near the unoccupied metal-binding site. To test the influence of the metal ions on the stability of the structure, we initiated three simulations in which Zn^{2+} was removed from the binding site, with the carboxylates in three different protonation states (table S4). In each simulation, the tight dimer interface remained at a constant, close distance, whereas the loose dimer interfaces separated by up to 5 Å (fig. S2B). The findings suggest that metal binding is important for stabilizing the tetrameric bundle but not the tightly packed dimer. Although these simulations are much shorter than the time scale required for a transport cycle, they are consistent with the intended design of loose and tight interfaces, each interface with distinct roles in facilitating the positioning of side chains and providing a dynamic waterlike path for ion motion through the center of the transporter.

We used a battery of techniques to define the structural and dynamic characteristics of Rocker. The binding of metal ions and oligomerization was studied in micelles by using analytical ultracentrifugation (AUC) and solution nuclear magnetic resonance (NMR). The structure of the Zn^{2+}-free state was determined at high resolution by x-ray crystallography of Rocker solubilized in both micelles and monoolein lipidic cubic phase. Finally, the oligomeric state, topology, and Zn^{2+} binding were determined in phospholipid bilayers by solid-state NMR (SSNMR).

AUC showed that Rocker forms tetramers in a Zn^{2+}-dependent manner in dodecylphosphocholine (DPC) micelles. Equilibrium sedimentation curves were well described by an equilibrium between a

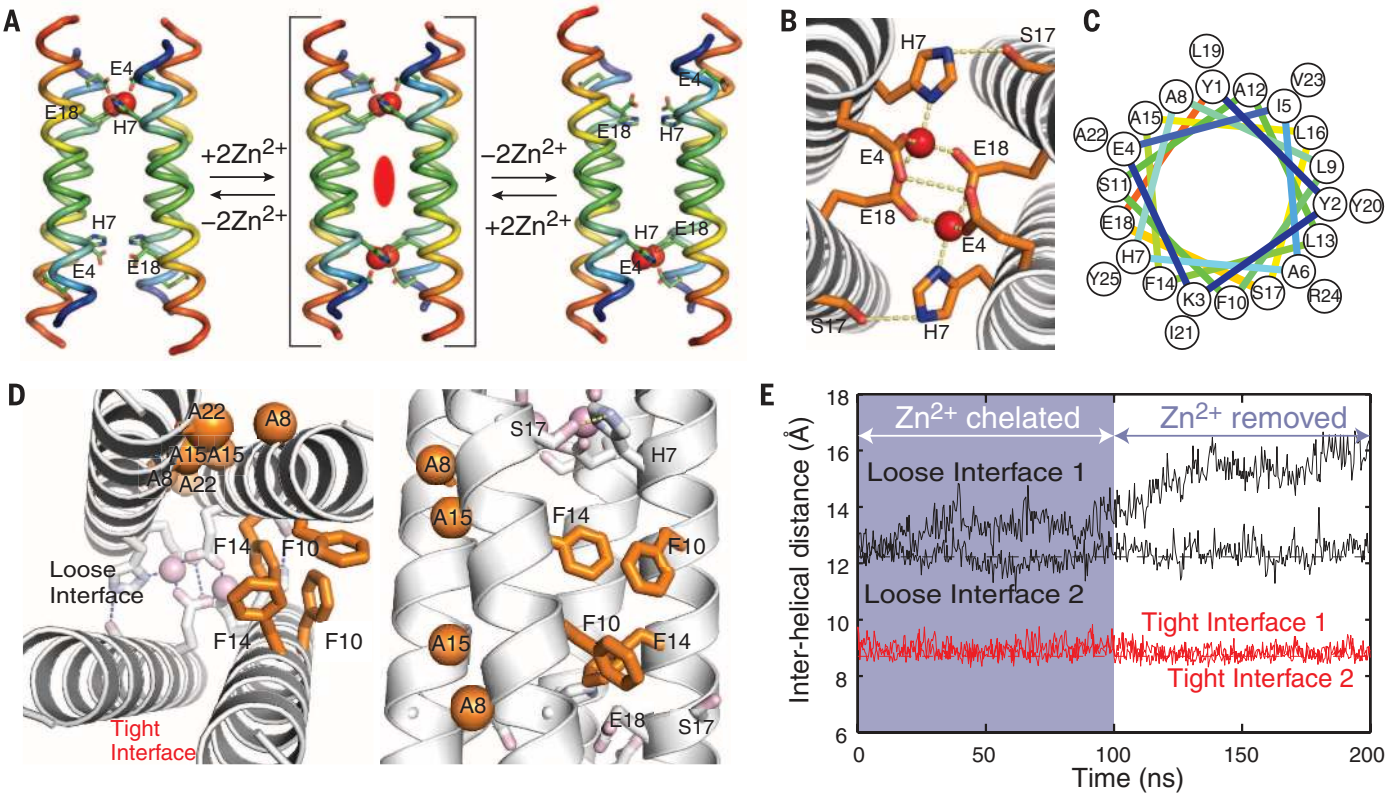

Fig. 1. Computational design and molecular dynamics simulations of Rocker. (**A**) Schematic of the goal of obtaining conformational exchange between two oppositely oriented symmetry-frustrated states without being trapped in a symmetric state with both sites simultaneously occupied. (**B**) Metal site consists of a set of ExxH motifs and a single Glu residue from each of the tight dimers. (**C**) Helical-wheel diagram of Rocker peptide. (**D**) The repacking algorithm placed Ala residues at the tight interface and Phe residues at the loose interface. Empty metal site on the left is omitted for clarity. (**E**) MD simulation of the design model with two Zn^{2+} ions placed at one metal site show stable interhelical distances for both tight and loose interfaces. Continuing the simulation after removing the Zn^{2+} ions maintained the tight interfaces, but resulted in an increased interhelical distance at the loose interface.

tight dimer and a tetramer (fig. S3). Tetramerization is dominant only at a peptide-to-detergent ratio of 1:200 or higher in this medium, but the addition of excess Zn^{2+} shifted the equilibrium toward the tetrameric state at lower peptide/detergent ratios (supplementary material).

We crystallized Zn^{2+}-free Rocker from micelles, as well as the lipidic cubic phase, in a total of three nonisomorphous space groups and solved structures using data that extended between 2.7 and 2.8 Å (Fig. 2). Only the non-Zn^{2+} form of the protein has crystallized to date. The crystallographic structures solved by molecular replacement show a dimer formed by two tightly packed helices (Fig. 2, A and B). The conformations of the dimer in the three structures are nearly identical (Cα RMSDs between 0.60 and 0.84 Å), despite differences in crystal packing. The dimers are composed of straight α helices that interact along the tight interface with tight interdigitation of the small methyl groups of the alanine residues, as in the design. The His and Glu ligands are positioned with the potential to bind metals with a change in rotameric state (Fig. 2, B and C). The observed structure of the dimer is in good agreement with the designed tight dimer (Cα RMSD ranges from 2.3 to 2.6 Å). We attribute small deviations from the design to the lack of metal-ligand interactions in the experimental structure. Indeed, in the MD simulations of the Zn^{2+}-free structure, the dimers move 0.8 Å closer to the x-ray structure than the original design (fig. S2C).

The binding stoichiometry for Zn^{2+} was confirmed in solution by titrating Rocker with Zn^{2+} ions in DPC micelles under conditions where it is predominantly tetrameric (peptide/detergent ratio = 1:100). Addition of Zn^{2+} resulted in a decrease in the intensities of aromatic resonances (including the chelating His residue) and an increase in a new set of peaks in the solution NMR spectra (Fig. 3A). The titration plateaus at two Zn^{2+} ions/tetramer. Two sets of peaks in the spectrum indicate that the rate of dissociation and rebinding of Zn^{2+} to the side chains is slower than ~10 ms. Beyond two equivalents, additional shifts are observed, but the change with respect to the Zn^{2+} concentration is more gradual and indicative of much weaker association of the metal ions with a second binding site. This behavior is consistent with the design, which anticipates negative cooperativity between the two sets of di-Zn^{2+}–binding sites.

Previous work with homo-tetrameric peptides shows that they are much more stable in phospholipid bilayers than DPC micelles (*32*, *33*), so we turned to SSNMR to determine the structure and conformational dynamics of Rocker in phospholipid bilayers. One-dimensional (1D) ^{13}C cross-polarization (CP) magic angle–spinning (MAS) spectra of apo-Rocker in dimyristoylphosphatidylcholine (DMPC) bilayers from −40° to 40°C showed a single set of relatively narrow peaks (0.9 ppm Cα line widths) per carbon for four ^{13}C-labeled residues (Fig. 3B). The backbone ^{13}C chemical shifts reflect helical structure (fig. S4C). The line widths broaden with increasing temperature, which indicates that the peptide becomes mobile in the liquid-crystalline phase of the membrane. Dipolar coupling measurements yield ^{13}C-H order parameters of 0.84/0.84, 0.73/0.77, and 0.55/0.75 for Cα at Ala8/Ala22, L19, and I5 in apo/Zn^{2+}-bound states, respectively (fig. S4B), and all dephasing curves are asymmetric, which indicates global microsecond–time scale motion in both the apo and Zn^{2+} bound peptides (*34*, *35*). The addition of Zn^{2+} ions had a strong influence on the SSNMR spectra of Rocker. In contrast to the apo sample, the Zn^{2+}-bound sample lacks the L19α-I5δ peak and has weaker A8/22-I5 and A8/22-L19 cross peaks, which indicate that Zn^{2+} binding loosens interhelical packing (Fig. 3C). Ion binding also caused noticeable chemical shift changes, which are particularly pronounced at A8 and A22 (Fig. 3C and fig. S4, D and E). Taken together, these results show a single conformation with substantial dynamics on the microsecond time scale and significant Zn^{2+}-dependent structural perturbations.

To determine the oligomeric structure in DMPC bilayers, we conducted a ^{19}F spin diffusion experiment, Centerband-Only Detection of Exchange (CODEX), on Rocker singly labeled with *para*-^{19}F-phenylalanine (^{19}F-Phe) at position 14 (*36*, *37*). Distance-dependent interhelical ^{19}F-^{19}F dipolar coupling is manifested as a decay of a ^{19}F spin echo with increasing mixing time. The equilibrium value of the spin echo intensity is $1/n$, where n is the oligomer number of the assembly. The measured ^{19}F CODEX intensities (Fig. 3D and fig. S5) decayed to <0.4, which indicates that the assembly is larger than a dimer. The nonplanar quadrilaterals formed by ^{19}F-Phe modeled in the anticipated tetramer superposed with the crystallographic dimers resulted in excellent fits of the measured decay (Fig. 3D and fig. S5). A C_4 symmetrical array of ^{19}F nuclei gave an unsatisfactory fit, which ruled out a square planar model (fig. S5E). These results corroborate an antiparallel tetramer.

Conclusive support for an antiparallel tetramer was obtained from 2D ^{13}C correlation spectra. At a mixing time of 500 ms, cross peaks between L19 and I5 side chains were observed (Fig. 3C). These residues are found along the tight dimer interface, and, together with the ^{19}F-Phe interaction along the loose interface, confirm antiparallel association along both interfaces in bilayers.

Finally, to determine whether the designed peptide is embedded in the lipid bilayer, we measured 2D NMR spectra that correlate the lipid and water ^{1}H signals with the peptide ^{13}C chemical shifts (*38*, *39*). Lipid-peptide cross peaks were detected at short mixing times (< 36 ms) (fig. S4F), which indicates that the peptide is well inserted into the hydrophobic part of the membrane. The fast spin–diffusion buildup curves for both the lipid and water ^{1}H peaks (fig. S4G) indicate that the Rocker helical bundle spans the membrane and is well hydrated, likely by both the membrane-surface water and intrachannel water.

Two important characteristics of natural transporters are their substrate-selectivity and their ability to use one substrate's concentration gradient to drive the uphill transport of a second substrate. To test how Rocker meets these criteria, we conducted flux assays in large unilamellar vesicles (LUVs) in which we monitored Zn^{2+} and H^{+} influx and efflux using fluorescent indicators (Fig. 4A and supplementary methods).

To test ion selectivity, we measured Rocker's ability to facilitate inward metal ion transport down a

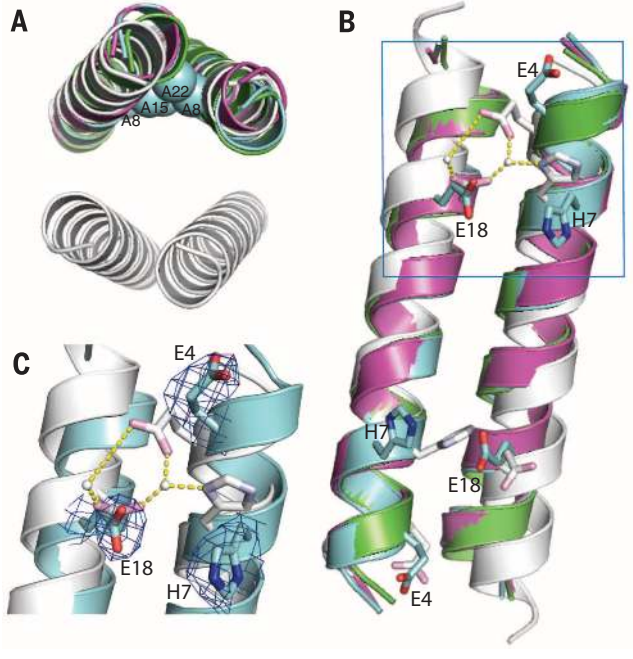

Fig. 2. Structure of Rocker. (**A**) Axial view of the x-ray crystal structures from three different packing environments (green, cyan, and magenta for space groups of increasing symmetries, $P4_32_12$, $I4_122$, and $I2_13$, respectively) superimposed on the tight dimeric subunit of the design model (white), with the Ala residues (spheres from the cyan structure with highest resolution of 2.7 Å) forming the tight interface as anticipated. (**B**) Metal-binding residues (sticks) from the crystal structures can chelate with a change in rotamers without encountering any unfavorable steric interactions within the dimer. (**C**) A close-up of the metal site with $2mF_{obs} - DF_{calc}$ map contoured at 1.0 σ for the 2.7 Å–resolution structure.

concentration gradient. As expected, Rocker conducts first-row transition metal ions Zn^{2+} and Co^{2+} but not the hard divalent ion, Ca^{2+}, which prefers higher-valent oxygen-rich ligand environments (Fig. 4B and fig. S6, A and B). Moreover, Ca^{2+} does not influence Zn^{2+} efflux (fig. S6A), and substitution of the Glu ligands to Gln greatly impairs Zn^{2+} efflux (Fig. 4B).

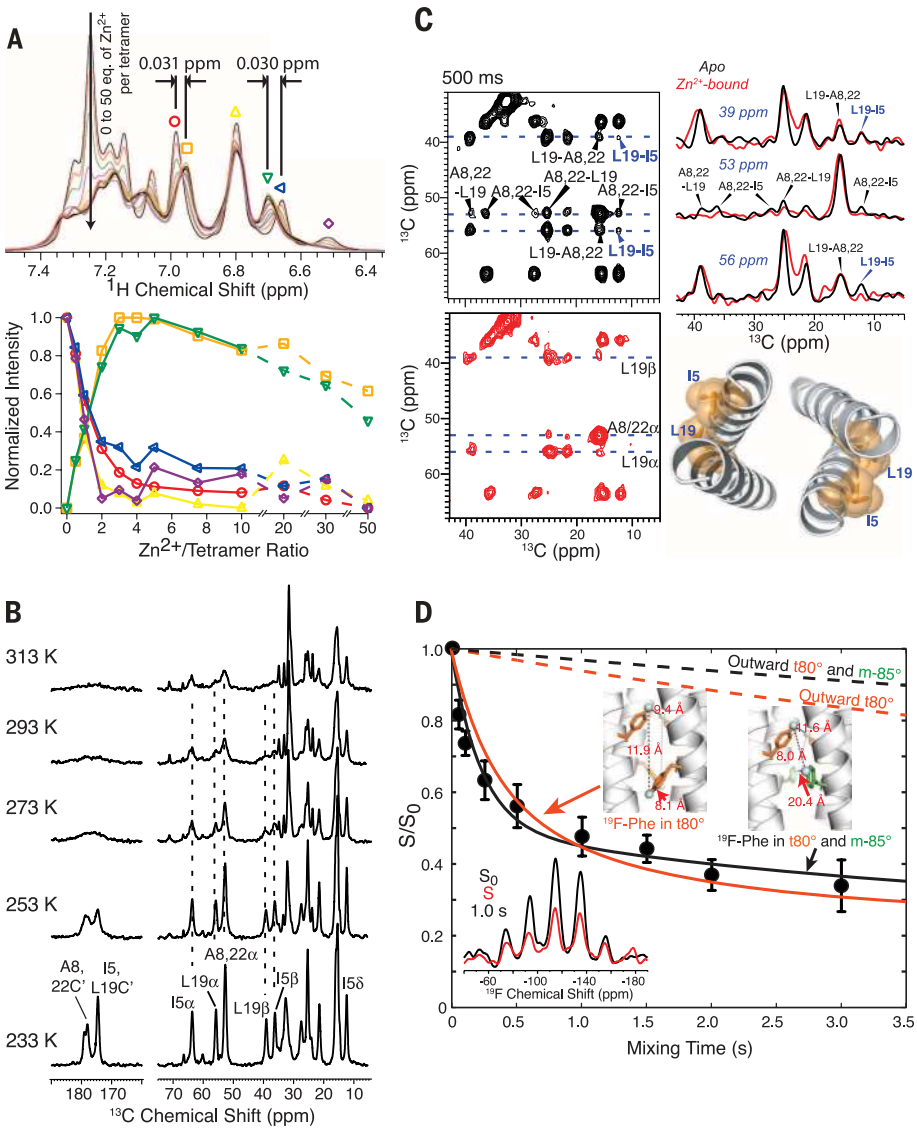

Fig. 3. Evidence for Zn^{2+} binding and tetramerization of Rocker in micelles and lipid bilayers. (**A**) ^{1}H-NMR of Rocker in D_2O and deuterated DPC (at 900 MHz ^{1}H field) shows significant changes to the side-chain chemical shifts as Zn^{2+} is titrated into the solution. The changes level off when Zn^{2+} reaches two equivalents per tetramer, which indicates the expected binding stoichiometry. (**B**) 1D ^{13}C CP-MAS spectra of apo Rocker in DMPC bilayers from 233 K to 313 K show invariant peak positions across a wide temperature range, which indicates single species with conformational dynamics in bilayers. (**C**) 2D ^{13}C-^{13}C 2D correlation spectra of apo and Zn^{2+} bound Rocker with 500-ms mixing. Relevant 1D cross sections are plotted to compare cross-peak intensities. L19-I5 cross peaks (blue annotations) are observed, indicating antiparallel packing. Compared with the apo sample, the Zn^{2+}-bound sample lacks the L19α-I5δ peak in the 56-ppm cross section and has much weaker A8/22-I5 and A8/22-L19 cross peaks, which indicate that Zn^{2+} binding loosens interhelical packing. The proximal L19 and I5 are shown on a structural model of Rocker. (**D**) ^{19}F CODEX data of DMPC-bound Rocker with *para*-^{19}F-Phe14 at 220 K and 8 kHz MAS (error bar, SD propagated from signal-to-noise). The CODEX intensity decays to 1/*n* of 0.34, where *n* is the oligomer number; this indicates that the peptide assembles into a species larger than dimers. The CODEX decay is well fit (solid lines) using ^{19}F-^{19}F distances found in inward-facing rotamers of Phe14 in an antiparallel tetramer, consistent with the crystal structures. The data rule out outward-facing orientations of Phe14 (dashed lines), which suggests that Glu4 and Glu18 face the pore.

The rate of Zn^{2+} transport into vesicles follows Michaelis-Menten kinetics (K_M = 280 ± 90 μM; V_{max} = 1.1 ± 0.1 min^{-1}). For comparison, the K_M and rate of transport in the natural ZitB Zn^{2+} transporter are 105 μM and 142 min^{-1}, respectively (*22*, *40*). From the Irving-Williams (*41*) series (which approximately predicts the relative affinities of first-row transition metal ions for a given site) and the ligand environment of Rocker, we expected that Co^{2+} should bind less tightly, which could lead to a higher K_M. Also, if ligand exchange is rate-limiting as suggested by the solution NMR spectra (Fig. 3A), the weaker binding affinity might be accompanied by an increase in V_{max}. Indeed, K_M for Co^{2+} increases to 1400 ± 200 μM and V_{max} increases to 470 ± 40 min^{-1} (Fig. 4, E and F, and fig. S6B).

We next tested Rocker's ability to cotransport Zn^{2+} and H^+. Rocker is able to use a Zn^{2+} gradient to drive the transport of protons uphill and into vesicles (Fig. 4C). Cotransport was measured by tracking both the downhill Zn^{2+} flux and the resulting H^+ flux as a function of the internal Zn^{2+} concentration. The rate of proton influx tracks with the rate of Zn^{2+} efflux, with a common K_M of 280 μM, which indicates that H^+ and Zn^{2+} transport are linked (Fig. 4, E and F). The proton-Zn^{2+} stoichiometry computed from the initial rates is three to four protons per Zn^{2+}. This finding is consistent with the guiding hypothesis that the binding of Zn^{2+} occurs with the concomitant displacement of protons. Moreover, Rocker functioned in a Zn^{2+}-proton antiport assay in the presence of a membrane permeable ion, NO_3^-, which eliminates the accumulation of electrical potentials (fig. S6C).

We also determined that a proton gradient is able to cause accumulation of Zn^{2+} up its own concentration gradient, when the initial concentrations of Zn^{2+} were identical on both sides of the vesicle. However, the efficiency of the process is far less than for the converse: Over 100 protons are transported for every Zn^{2+} transported. This finding suggests that there might be two competing mechanisms: The predominant one is diffusion of protons through Zn^{2+}-bound Rocker; the less-frequent path involves proton binding at the Zn^{2+} site and expulsion of a zinc ion. A possible explanation for the different behavior for Zn^{2+} compared with proton gradients is that the highly polar divalent Zn^{2+} is unable to diffuse through Rocker without binding to the coordination sites, which in turn would require deprotonation of the ligands. By contrast, protons could move along proton wires through the pore without requiring dissociation of the divalent metal ion. A possible reason for the proton-leakiness is the lack of a proton-impermeable hydrophobic gate, which appears to be important for tight coupling in much larger and highly evolved proton-dependent transporters. Future designs will aim to achieve a transporter function similar to that of native proteins. Nevertheless, these findings, along with the very simple structure of Rocker, provide support for the view that

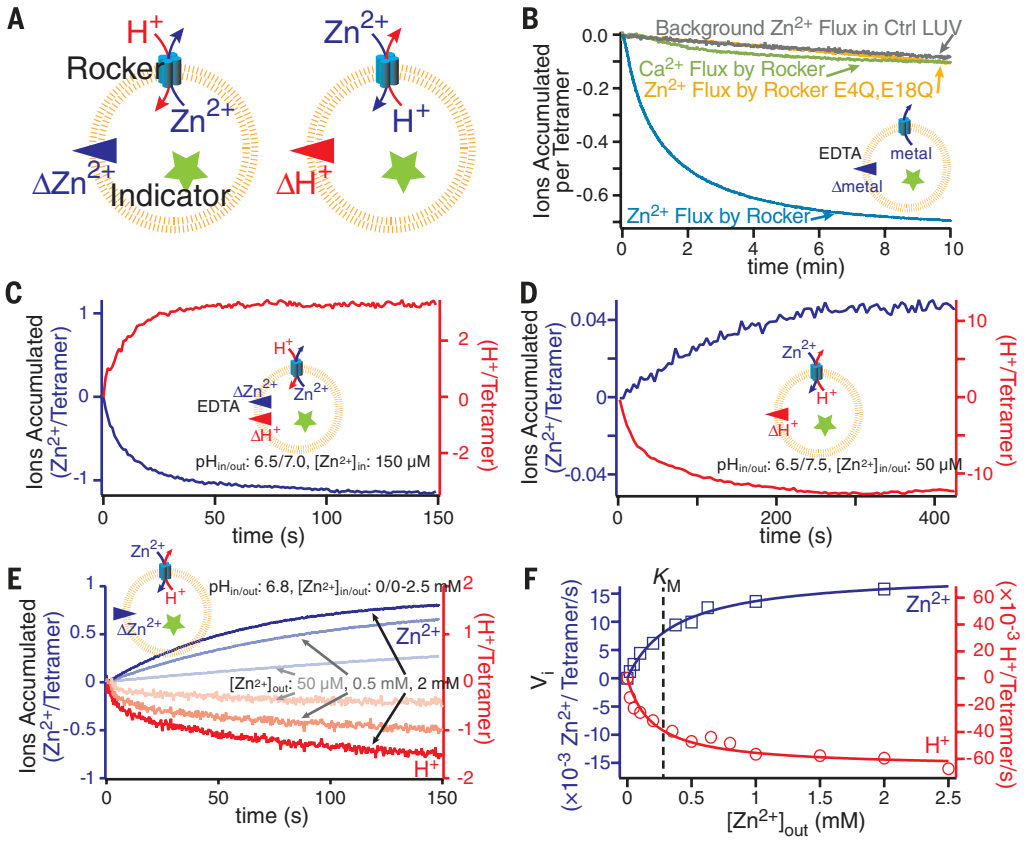

Fig. 4. Antiporter-like function of Rocker. (**A**) Examples of liposome flux assays using fluorescent indicators for characterizing the cotransportation function are illustrated. (**B**) Ion selectivity in Rocker is shown via a Zn^{2+} efflux assay. Rocker can specifically transport Zn^{2+} (blue) but not Ca^{2+} (green), at a level higher than passive leakage (gray). Mutating the first-shell ligands via E4/E18-to-Q substitutions abrogates Zn^{2+} transport (gold). (**C**) Rocker-mediated, outward [Zn^{2+}] gradient-driven proton-antiport against an outward pH gradient is shown by measuring net inward proton flux (red, right axis) and the outward Zn^{2+} flux (blue, left axis). (**D**) Rocker-mediated, H^+-driven Zn^{2+} antiport under symmetrical Zn^{2+} concentration is shown using both the outward proton flux (red, right axis) and the inward Zn^{2+} flux (blue, left). (**E**) Representative traces show the dependence of initial rates of transport on the exterior Zn^{2+} concentration. (**F**) The initial rates of transport of Zn^{2+} and H^+ from panel (E) increase with increasing exterior Zn^{2+} concentration, following Michaelis-Menten kinetics with a K_M of ~ 280 μM. (Error values in text are SD propagated from curve fitting.)

transporters may have evolved from very simple pseudo-symmetric precursors (*42*).

The structural and functional characterization of Rocker indicates that the design community has now passed an important milestone; the first high-resolution structure of a designed membrane protein has been determined through a combination of x-ray crystallography and NMR. Our design strategy combined the strengths of traditional computational design techniques with biophysically motivated conformational ensemble–based reasoning. Although Rocker's activity falls short of natural transporters, it remains significant that function was achieved without high-throughput screening or directed evolution—and bodes well for future investigations in which computational design is combined with these powerful experimental methods.

REFERENCES AND NOTES

1. N. Koga *et al.*, *Nature* **491**, 222–227 (2012).
2. M. L. Zastrow, V. L. Pecoraro, *Coord. Chem. Rev.* **257**, 2565–2588 (2013).
3. C. E. Tinberg *et al.*, *Nature* **501**, 212–216 (2013).
4. A. J. Reig *et al.*, *Nat. Chem.* **4**, 900–906 (2012).
5. M. L. Zastrow, A. F. A. Peacock, J. A. Stuckey, V. L. Pecoraro, *Nat. Chem.* **4**, 118–123 (2012).
6. M. L. Zastrow, V. L. Pecoraro, *J. Am. Chem. Soc.* **135**, 5895–5903 (2013).
7. G. Kiss, N. Çelebi-Ölçüm, R. Moretti, D. Baker, K. N. Houk, *Angew. Chem. Int. Ed. Engl.* **52**, 5700–5725 (2013).
8. I. V. Korendovych *et al.*, *J. Am. Chem. Soc.* **132**, 15516–15518 (2010).
9. J. M. Perez-Aguilar, J. G. Saven, *Structure* **20**, 5–14 (2012).
10. S. Radestock, L. R. Forrest, *J. Mol. Biol.* **407**, 698–715 (2011).
11. O. Jardetzky, *Nature* **211**, 969–970 (1966).
12. P. Mitchell, *Nature* **180**, 134–136 (1957).
13. E. A. Morrison *et al.*, *Nature* **481**, 45–50 (2012).
14. W. F. DeGrado, Z. R. Wasserman, J. D. Lear, *Science* **243**, 622–628 (1989).
15. J. D. Lear, Z. R. Wasserman, W. F. DeGrado, *Science* **240**, 1177–1181 (1988).
16. M. Hong, W. F. DeGrado, *Protein Sci.* **21**, 1620–1633 (2012).
17. A. Pasternak, J. Kaplan, J. D. Lear, W. F. Degrado, *Protein Sci.* **10**, 958–969 (2001).
18. F. H. C. Crick, *Acta Crystallogr.* **6**, 685–689 (1953).
19. G. Grigoryan, W. F. Degrado, *J. Mol. Biol.* **405**, 1079–1100 (2011).
20. C. M. Summa, A. Lombardi, M. Lewis, W. F. DeGrado, *Curr. Opin. Struct. Biol.* **9**, 500–508 (1999).
21. A. Lombardi *et al.*, *Proc. Natl. Acad. Sci. U.S.A.* **97**, 6298–6305 (2000).
22. Y. Chao, D. Fu, *J. Biol. Chem.* **279**, 17173–17180 (2004).
23. G. Grigoryan, A. W. Reinke, A. E. Keating, *Nature* **458**, 859–864 (2009).
24. G. Grigoryan, *J. Comput. Chem.* **34**, 2726–2741 (2013).
25. T. Lazaridis, *Proteins* **52**, 176–192 (2003).
26. A. Senes *et al.*, *J. Mol. Biol.* **366**, 436–448 (2007).
27. C. A. Schramm *et al.*, *Structure* **20**, 924–935 (2012).
28. C. M. Summa, M. M. Rosenblatt, J. K. Hong, J. D. Lear, W. F. DeGrado, *J. Mol. Biol.* **321**, 923–938 (2002).
29. Y. Zhang, D. W. Kulp, J. D. Lear, W. F. DeGrado, *J. Am. Chem. Soc.* **131**, 11341–11343 (2009).
30. S. Unterreitmeier *et al.*, *J. Mol. Biol.* **374**, 705–718 (2007).
31. D. T. Moore, B. W. Berger, W. F. DeGrado, *Structure* **16**, 991–1001 (2008).
32. L. Cristian, J. D. Lear, W. F. DeGrado, *Proc. Natl. Acad. Sci. U.S.A.* **100**, 14772–14777 (2003).
33. K. R. MacKenzie, K. G. Fleming, *Curr. Opin. Struct. Biol.* **18**, 412–419 (2008).
34. E. R. deAzevedo *et al.*, *J. Chem. Phys.* **128**, 104505 (2008).
35. M. F. Cobo, A. Achilles, D. Reichert, E. R. Deazevedo, K. Saalwächter, *J. Magn. Reson.* **221**, 85–96 (2012).
36. E. R. deAzevedo, W.-G. Hu, T. J. Bonagamba, K. Schmidt-Rohr, *J. Am. Chem. Soc.* **121**, 8411–8412 (1999).
37. J. J. Buffy, A. J. Waring, M. Hong, *J. Am. Chem. Soc.* **127**, 4477–4483 (2005).
38. D. Huster, X. Yao, M. Hong, *J. Am. Chem. Soc.* **124**, 874–883 (2002).
39. M. Hong, *Structure* **14**, 1731–1740 (2006).
40. Y. Chao, D. Fu, *J. Biol. Chem.* **279**, 12043–12050 (2004).
41. R. J. P. W. H. Irving, R. J. P. Williams, *J. Chem. Soc.* 3192–3210 (1953).
42. M. Rapp, E. Granseth, S. Seppälä, G. von Heijne, *Nat. Struct. Mol. Biol.* **13**, 112–116 (2006).

ACKNOWLEDGMENTS

Authors acknowledge J. Holton and G. Meigs at The Lawrence Berkeley National Laboratory Advanced Light Source 8.3.1; K. Rajashankar, S. Banerjee, and I. Kourinov at Argonne National Laboratory Advanced Photon Source Northeastern Collaborative Access Team for technical support in x-ray data collection; and O. P. Choudhary and J. L. Adelman at the University of Pittsburgh for helpful discussions regarding the simulations. Simulations were carried out in part with XSEDE resources through grant MCB080011 to M.G. This work was supported by NIH F32 GM096727 to N.H.J., The Jane Coffin Childs postdoctoral fellowship to MPB; Ramalingaswami Fellowship from the Department of Biotechnology, India, to R.A.; NIH R01 GM089740 to M.G.; NIH R01 GM088204 to M.H.; Alfred P. Sloan Foundation Research Fellowship to G.G.; NIH R01 GM054616 to W.F.D.; and NSF DMR 1120901 (W.F.D.). The coordinates for the x-ray structures with space groups, $P4_32_12$, $I4_122$, and $I2_13$, are deposited in the Protein Data Bank (PDB) with accession codes, 4P6J, 4P6K, and 4P6L, respectively. The SSNMR structure is deposited in PDB with an accession code, 2MUZ.

SUPPLEMENTARY MATERIALS

www.sciencemag.org/content/346/6216/1520/suppl/DC1
Materials and Methods
Figs. S1 to S6
Tables S1 to S5
References (*43*–*67*)

12 September 2014; accepted 21 November 2014
10.1126/science.1261172

De novo design of a transmembrane Zn^{2+}-transporting four-helix bundle

Nathan H. Joh *et al.*

Science **346**, 1520 (2014);
DOI: 10.1126/science.1261172

Science (print ISSN 0036-8075; online ISSN 1095-9203) is published weekly, except the last week in December, by the American Association for the Advancement of Science, 1200 New York Avenue NW, Washington, DC 20005.

www.sciencemag.org/content/346/6216/1520/suppl/DC1

Supplementary Materials for

De novo design of a transmembrane Zn transporting four-helix bundle

Nathan H. Joh, Tuo Wang, Manasi P. Bhate, Rudresh Acharya, Yibing Wu, Michael Grabe,* Mei Hong,* Gevorg Grigoryan,* William F. DeGrado*

*Corresponding author. E-mail: william.degrado@ucsf.edu (W.F.D.); gevorg.grigoryan@darthmouth.edu (G.G.); meihong@mit.edu (M.H.); michael.grabe@ucsf.edu (M.G.)

Published 19 December 2014, *Science* **346**, 1520 (2014)
DOI: 10.1126/science.1261172

This PDF file includes

Materials and Methods

I. Computational Design

Designable four-helix bundles for Zn^{2+} binding

In choosing the zinc coordination topology for Rocker we were inspired by the binding geometry in an artificial di-manganese four-helix bundle(*43*) (see **Fig. S1A**). In this protein two metal ions are coordinated with four Glu and two His residues, with crucial second shell hydrogen bonds to aspartates helping position the histidines for metal coordination. We noticed that swapping coordinating residues between two adjacent helices could produce a D2-symmetric binding geometry topologically suitable for our design purposes (see **Fig. S1B**). Since we intended our transporter to be membrane soluble, we replaced the second-shell interacting Asp with a Ser. Having chosen this general arrangement of residues, we now needed to tune the bungle geometry to optimize both the favorability of Zn binding and the designability of helix-helix interfaces. For this purpose, we performed a stochastic search over the space of Crick parameters for a D2-symmetric anti-parallel tetrameric coiled-coil(*19*). Chain length was set to 25 residues to enable a single pass through the bilayer. Starting parameters were set based on frequent values for this topology seen in our previous study(*19*), namely $R_0 = 7.465$ Å (superhelical radius), $\omega_0 = -3.554$ °/res (superhelical frequency), $\Delta\varphi_0 = -95°$ (superhelical phase offset between chains of opposite orientation), $\varphi_1 = 250.1°$ (starting helical phase), and $\Delta Z_{\text{off}} = -2.248$ Å (axial offset between chains of opposite orientation); see (*19*) for parameter definitions. We reasoned that placing di-Zn^{2+} binding sites near the ends of the bundle would maximize recruitment of ions from solution, so residues 4 and 7 on chains running in one direction ("up" chains) were designated for Glu and His, respectively, whereas residues 17 and 18 on adjacent chains (running in opposite direction; "down" chains) for Ser and Glu, respectively. Parameters d (helical rise per residue), R_1 (helical radius), and ω_1 (helical frequency) were kept fixed throughout the search at their ideal values of 1.51 Å, 2.26 Å, and 102.867 °/res, respectively. The pitch angle α was calculated for every structure sampled as $\alpha = \arcsin(R_0\omega_0 d^{-1})$. The search was performed in Matlab using the unconstrained optimization function *fminunc* over the non-fixed parameters $\{R_0, \omega_0, \Delta\varphi_0, \varphi_1, \Delta Z_{\text{off}}\}$. For each sampled set of parameters, the corresponding all-Ala structure was generated and binding-site histidines were built in the correct rotamer (taken from 1LT1 binding site) with pre-attached Zn (the position of Zn relative to His taken from 1LT1). Rotameric degrees of freedom of remaining binding-site residues (four Glu and two Ser residues) were enumerated assuming strict D2 symmetry. The total *in-vacuo* energy of the binding site (internal energy of binding site residues and zinc and their interaction with the rest of the structure, E_{bs}) and the total internal energy of the remainder of the structure (template energy, E_t) were calculated using the CHARMM force-field (parameter set 22) for each rotameric combination. The final score for a structure was the minimum of $(max(E_t + 10, 0) + E_{bs})$ over rotameric combinations. That is, unless the template energy became high (above -10 kcal/mol, indicating steric clashes), the score was the binding site energy. The parameters with the lowest score found were $\{R_0 = 7.5\text{ Å}, \omega_0 = -1.994\text{ °/res}, \Delta\varphi_0 = -106.82°, \varphi_1 = -111.96°, \Delta Z_{\text{off}} = -2.386\text{ Å}\}$ and were used to generate the symmetric state template (**Fig. S1C**). To generate the asymmetric state, chains of the symmetric template were replaced with ideal α-helices by minimizing the Cα root-mean-square-deviation of residues 4 through 7 for up chains and residues 17 through 19 for down chains (see **Fig. S1D**). This left the binding site at one end of the asymmetric bundle essentially unchanged, while it flared the other end of the bundle such that Zn^{2+} binding could no longer occur. The designability of both symmetric and asymmetric

templates was verified by finding close structural matches in the PDB to the two topologically different interfaces in both bundles. For this purpose, dimeric fragments of each interface, covering 12 residues in each chain, were analyzed via MaDCaT (*44*) (see Fig. **S1E-F**). The two templates were used as input into a two-state protein design framework.

Two-state Protein Design

Alphabet

The design alphabet (see Table S1) was guided by the membrane depth and functional requirements of different regions. Binding-site positions 4, 7, 17, and 18 were fixed to Glu, His, Ser, and Glu, respectively. Histidines were avoided in all positions (except 7) to help with the specificity of Zn^{2+} binding in the intended site. Hydrophobic, polar, and charged residues were allowed in the "vestibule" of the transporter (i.e., residues near the water/membrane interface) where they may be needed to stabilize incoming ions or form favorable interactions with lipid head groups or binding-site residues. Regions deeper in the membrane were allowed polar and hydrophobic residues only (and not charged ones), while regions close to the center of the membrane were allowed only hydrophobic residues along with Ser and Thr. Positions 8, 15, and 22 had a strong preference for Ala in the structural neighbors to the narrow interface returned by MaDCaT (in both symmetric and asymmetric templates), so only Ala was allowed in these positions during design.

Table S1. Overall design alphabet.

Position	Allowed amino acid choices
1	A; G; S; T; V; L; I; M; F; Y; W; N; Q; K
2	A; G; S; T; V; L; I; M; F; Y; W; N; Q; K
3	A; G; S; T; V; L; I; M; F; Y; W; D; E; N; Q; K; R
4	E
5	A; S; T; V; L; I; M; F; Y; W; Q
6	A; G; S; T; V; L; I; M; F; Y; W; N; Q; K
7	H
8	A
9	A; S; T; V; L; I; M; F; Y; W; Q
10	A; G; S; T; V; L; I; M; F; Y; W; N; Q; K
11	A; G; S; T; V; L; I; M; F; Y; Q
12	A; G; S; T; V; L; I; M; F; Y; W
13	A; G; S; T; V; L; I; M; F; Y; W
14	A; G; S; T; V; L; I; M; F; Y; W
15	A
16	A; G; S; T; V; L; I; M; F; Y; W

17	S
18	E
19	A; S; T; V; L; I; M; F; Y; W
20	A; S; T; V; L; I; M; F; Y; W
21	A; G; S; T; V; L; I; M; F; Y; W; N; Q; K
22	A
23	A; G; S; T; V; L; I; M; F; Y; W; N; Q; K
24	A; G; S; T; V; L; I; M; F; Y; W; D; E; N; Q; K; R
25	A; G; S; T; V; L; I; M; F; Y; W; D; E; N; Q; K; R

Energy function

Rotameric self and pair energies for design calculations were computed in CHARMM 31 using the IMM1 force-field in the united atom model (param 19) (*25*), except that van der Waals radii were reduced to 90% of their size. Within IMM1, the solvent "water" was used to model the aqueous solution and solvent "chex" to model the membrane, with all parameters left at their default values, including 30 Å for the width of the interior membrane region with transition between the interior and exterior occurring over 10 Å. Prior to calculation, templates were placed in the center of the membrane with their largest principal components normal to the membrane. The Richardson & Richardson penultimate rotamer library was used (*45*). The design stages outlined below involve different sequence space searches, where for each sequence sampled the optimal rotameric configuration is found using a combination of DEE/A* algorithms(*46*) and the resulting structure is subjected to post-evaluation for scoring.

Sequence Design

The goal was to find candidate sequences that may prefer the asymmetric state based on simple packing considerations and are predicted to stably insert into the bilayer. A Monte Carlo (MC) search was conducted in the full sequence space, with 32 independent trajectories with random starting points each visiting 1,500 sequences (a move involved a random mutation at a random site). Temperature was dropped linearly from 1,000 K to 200 K over the length of the trajectory. Upon finding the optimal rotameric configuration as described above, each structure was subjected to short continuous side-chain minimization in CHARMM 31 using the IMM1 force-field, with 100% van der Walls radii (10 steps of steepest-descent followed by 10 steps of adopted basis Newton-Raphson minimization) and its total conformational energy under IMM1 was calculated. Further, the energy of inserting the bundle into the middle of the bilayer (E_{ez}), along with its optimal depth of insertion (d_{ez}), were calculated using the Ez potential(*26*). The objective function optimized in MC was:

$$f = \frac{1}{1+\exp[-\beta(\{E_s - E_a\} - \Delta E_{cut})]} \cdot \frac{1}{1+\exp[-\beta_{ez}(E_{ez}^{cut} - E_{ez})]} \cdot \exp(-\beta_d d_{ez}) \cdot E_a,$$

Where E_s and E_a are the energies of the symmetric and asymmetric states, respectively, ΔE_{cut} is a threshold for the desired gap between the two states (favoring the latter), E_{ez}^{cut} is a threshold Ez membrane insertion energy, and β, β_{ez}, and β_d are temperature factors for conformational energy, Ez insertion energy, and optimal insertion depth, respectively. Parameter values used

were $\Delta E_{cut} = 50$ kcal/mol, $E_{ez}^{cut} = -5$ (set roughly equal to the Ez insertion energy of the transmembrane region of the M2 proton channel — a tetrameric bundle similar to our design in size and the need to employ some polar and charged residues for function), $\beta = 0.3$ mol/kcal, $\beta_{ez} = 0.2$, $\beta_d = 0.125$ Å^{-1}. The objective function can be interpreted as requiring a significant preference for the asymmetric state, a favorable energy of insertion into the bilayer, and a preference for the geometric center of the bundle to lie close to the central plane of the bilayer. If any of these conditions are not met, the objective function quickly vanishes. Provided that all of these requirements are met, sequences with more favorable conformational energies in the asymmetric state are preferred.

Our experience with more substantial relaxation in post-evaluating rotameric structures was that the only sequences that produced lower energies in the asymmetric state were those that had considerable side-chain strain post-minimization (e.g., strongly deviating bond angles and lengths) but had even more strain and steric clashes in the symmetric state. We reasoned that simple minimization would not be able to capture preferences between these two subtly different structural states, so we opted for minimal relaxation with the aim of discovering packing arrangements that may encode preference for the asymmetric state.

Since our design would encounter both lipid and aqueous environments, it was not trivial to formulate a relevant and tractable reference (unfolded) state model, so no explicit reference state energy was computed here. We felt this was reasonable given that the objective function was largely driven by specificity terms (i.e., water versus membrane solubility or preference for the symmetric versus asymmetric states), to which the reference state does not contribute.

Upon the completion of the above MC sampling, an additional four trajectories, each with 1,500 sampled sequences and temperatures scaling from 400 to 200 K, were run to sample more thoroughly bilayer-facing and near terminal positions (namely, positions 3, 5, 9, 13, 19, 20, and 21). The top scoring sequence from all of these trajectories (YYKEIAHALFSALFALSELYIAVRY) was inspected manually and four positions were identified as likely critical for controlling the preference for symmetry versus asymmetry: positions 10, 11, and 14 (located towards the middle "pivot" section of the bundle and pointing inward) and position 19 (a position near the end of the bundle along the narrow interface, with the potential to make different interactions in the "open" versus "closed" ends of the asymmetric state). Because of the abovementioned potential limitations of a simple side-chain packing procedure in encoding specificity between subtly different states, we sought to elaborate on these positions, generating a large number of candidates to be rescored with a more physically realistic approach. Specifically, we considered all combinations of $\{\mathrm{A, N, Q, L, K, M, F, S, or\ Y}\}$ in position 10, $\{\mathrm{A, Q, G, M, F, S, or\ T}\}$ in position 11, $\{\mathrm{A, I, M, F, S, T, Y, or\ V}\}$ in position 14, and $\{\mathrm{L\ or\ S}\}$ in position 19 in the background of the top sequence from above (a total of 1,008), building a structure for each for further rescoring as outlined below.

VALOCIDY-based calculations

All 1,008 sequences from above were predicted to have a large energetic preference for the asymmetric state based on a conformational energy upon a simple side-chain relaxation protocol. Because our design concept hinged upon the ability of the sequence to have at least some preference for the asymmetric state, preventing it from becoming fully loaded with Zn and not transporting, we wanted to verify this conformational preference using a free energy-based method. For this purpose, we defined thermodynamic states around both the symmetric and asymmetric templates and applied the VALOCIDY approach(*24*) to calculate the absolute free

energy of both for each sequence, enabling a direct comparison between the two. The symmetric state was defined around the symmetric template using the following constraints: 1) Cα atoms of residues 4, 7, and 18 (residues in direct contact with Zn) were constrained to be within 1.5 Å of their initial location at both ends of the template and 2) φ/ϕ dihedral angles were constrained to be within 30° of their values in the template. The asymmetric state was defined around the asymmetric template by applying the following conditions: 1) Cα atoms of residues 4, 7, and 18 (residues in direct contact with Zn) were constrained to be within 1.5 Å of their initial location at only the narrow (Zn-bound) end of the template, 2) φ/ϕ dihedral angles were constrained to be within 30° of their values in the template, and 3) at the wide (Zn-free) end of the bundle, the distance between Cα atoms of residues 4 on diagonally opposing chains was constrained to be above 12 Å. This latter condition ensured that a Zn binding site could not be formed at the flared end of the asymmetric state. Table 2 summarizes state definitions and the restraints used in VALOCIDY to ensure thorough sampling of these.

Each of the 1,008 sequences was subjected to VALOCIDY calculations in each state, using four independent MD trajectories (run in CHARMM 31 with the IMM1 force-field at the constant temperature of 298.15 K maintained by a Nose-Hoover thermostat), each with 10 ns of equilibration followed by 100 ns of data collection. Snapshots were collected every 100 fs. Integration to obtain estimates of F_a and F_s, absolute free energies of the asymmetric and symmetric states, respectively, was performed using the bond-angle-torsion (BAT) coordinate system(*47*) as described previously(*24*). Means over the four integration runs were used as the final estimates, with standard error used to assess stochastic error. As is apparent from Fig. S1G, according to the estimated $\Delta F = F_s - F_a$, the majority of sequences previously believed to be selective for the asymmetric state, in fact switch their preference when evaluated thermodynamically by VALOCIDY. It is important to note that the IMM1 force-field likely provides a poor representation of interactions within the binding site itself, so the free energy differences computed here should be treated only as guides as to the relative conformation preferences between different sequences. Nevertheless, the very significant differences between predictions of the traditional computational design phase and the free energy-based rescoring by VALOCIDY clearly demonstrate limitations of semi-static rotamer-based scoring approaches for encoding conformational preferences. In fact, VALOCIDY predicted that the symmetric state was always preferred in terms of enthalpy (see Fig. S1H), meaning that the unfavorable steric interactions engineered in design to disfavor the symmetric state were not robust in the context of a wider ensemble. However, the conformational entropy was higher in the asymmetric state and sufficiently higher for a handful of sequences to tip the balance towards asymmetry (see Fig. S1G).

Manual inspection of sequences with the largest ΔF revealed an "over-crowding" effect—i.e., packing of aromatic residues in the hinge region of the bundle provided entropic destabilization of the symmetric state. We reasoned that such packing might make it difficult for Zn^{2+} ions to diffuse across the protein towards the opposing binding site, potentially severely slowing down or inhibiting transport. We judged that choosing a Ser at position 11 of the hinge region may both provide sufficient space for Zn^{2+} diffusion and may provide some polar stabilizing interactions with the ions as they travel through the bundle. We thus focused on all sequences with Ser at position 11, picking the one with the largest ΔF as the sequence to test experimentally. This was the sequence YYKEIAHALFSALFALSELYIAVRY, designated as Rocker (transmembrane translocation kinetics enhancer).

Table S2. Restraints used to define the symmetric and asymmetric states. A flat-bottom semi-harmonic potential was applied to each restraint, with the given force constant, such that the constraint became non-zero when the given degree of freedom came closer than the stated margin from its limiting value. See (*24*) for details of implementation**.**

Constraint Description	Margin	Force Constant	Sym[a]	Asym[b]
φ/ϕ angles within 30 ° of starting values	3°	$1{,}000\ {}^{kcal}/_{mol \cdot rad^2}$	YES	YES
Cα atoms of residues 4, 7, and 18 within 1.5 Å of starting location in the template	0.5 Å	$100\ {}^{kcal}/_{mol \cdot Å^2}$	YES	NO
Cα atoms of residues 4, 7, and 18 on wide side only within 1.5 Å of starting location	0.5 Å	$100\ {}^{kcal}/_{mol \cdot Å^2}$	NO	YES
Distance between Cα atoms of positions 4 (wide end of the bundle) to be above 12 Å.	0.5 Å	$100\ {}^{kcal}/_{mol \cdot Å^2}$	NO	SYM

[a,b] – these columns designate whether any given restrain was applied in the symmetric or asymmetric state, respectively.

II. Molecular Dynamics Simulations

We carried out four initial 100 ns simulations of the *in-silico* designed model predicted transporter embedded in a pure POPC bilayer. The transporter is a homo-tetramer with each chain consisting of 25 amino acids, and each chain labeled P1-P4.

Each simulation had two Zn^{2+} bound in one putative binding site, and the other site was empty. The residues in the Zn^{2+}-bound site had standard protonation states at pH 7.0 with the His7 residues protonated on the ε-nitrogen. The zinc free site had four different protonation schemes, expressed in Builds 1-4, shown in Table S1. We also carried out one 50 ns simulation of a fully zinc free system, termed the apo simulation, starting from the end of the build 1 simulation.

The protein was embedded in the membrane and solvated using the CHARMM-GUI webserver. The models were parameterized with the CHARMM 36 force field with CMAP corrections for the protein, the CHARMM 36 parameter set for lipids (*48*), and the Zn^{2+} non-bonded representation developed by Stote and Karplus (*49*). The ionic solution was adjusted for each build to impose electroneutrality attempting to keep the salt close to 100 mM NaCl. There are ~25,000 atoms in the finally systems. All simulations were performed with NAMD 2.9 (*50*). Heating and equilibration were carried out over 4.3 ns starting with restraints on all protein heavy atoms and the bound Zn^{2+} ions. First, the system was minimized for 2000 steps with restraints on all protein heavy atoms and the Zn^{2+} ions (k = 5 kcal/mol/Å^2). Next, the system was heated to 303 K over 0.3 ns in the presence of the same restraints. An initial equilibration trajectory was run for 2 ns using a reduced spring constant of k = 1 kcal/mol/Å^2 on all heavy atoms and the Zn^{2+}. Next, restraints were released on the side chain atoms, and the system was equilibrated for an additional 2 ns while still restraining the backbone and Zn^{2+} ions (k = 1 kcal/mol/Å^2). Water was not allowed to penetrate into the membrane region during the 4 ns of equilibration, but it was allowed to penetrate into the transporter.

The apo system was simulated starting from the end of the 100 ns simulation of the build with the same number. Zn^{2+} was removed from the binding site, the protonation state of glutamates in the zinc binding site were modified as stated in **Table S3**, ions were added to

solution to enforce charge neutralization, and new structure and topology files were generated with the psfgen plugin to VMD. The system was minimized, heated, and equilibrated in the same manner as builds 1-4, except no forces were applied to water during the equilibration steps.

Distribution of water molecules in the central pore was compiled from each of 100 ns simulation with snapshots separated by 0.4 ns. Prior to binning, the protein was centered along the z-axis using the Cα atom of Ser11 from Chain 1 as a reference. Bins were 3-Å wide, centered at the origin.

Table S3. Protonation schemes for residues in the apo site for MD simulations of Zn^{2+}-bound Rocker.

Scheme	E4 (P2/P4)	E18 (P1/P3)	Charge at zinc free site	Net Charge
Build 1	-	-	-2	0
Build 2	Protonated	-	0	+2
Build 3	Protonated	Protonated	+2	+4
Build 4	-	Protonated	0	+2

The dash (-) indicates standard protonation states, which is negatively charged for E4 and E18. The histidine residues in the apo site were kept neutral with protons on the □ nitrogen. E binding site is made up of two residues from two adjacent chains of the transporter. In each build we impose the same protonation state on both residues (chains P2/P4 for E4 and chains P1/P3 for E18). The last column indicates the net charge in the zinc free site of the protein. There are two basic residues in the vicinity (K3 (P2/P4)) and 4 acidic residues (E4 (P2/P4) and E18 (P1/P3)). Each build changes the local net charge as indicated.

Table S4. Protonation schemes for residues in metal site for MD simulations of apo Rocker.

Scheme	E4 (P1/P3)	E18 (P2/P4)	Net charge zinc free site
Build apo 1.1	-	-	-2
Build apo 1.2	Protonated	-	0
Build apo 3	Protonated	Protonated	+2

III. Materials

Peptides were synthesized as C-terminal amides using Fmoc solid-phase chemistry and purified as trifluoroacetate salts by HPLC using a C4 reverse-phase prep column. Lyophilized peptides were then dissolved in ethanol or isopropanol stock for reconstitution in experiments.

Reagents used in experiments include POPC (1-palmitoyl-2-oleoyl-*sn*-glycero-3-phosphocholine), POPG (1-palmitoyl-2-oleoyl-*sn*-glycero-3-phospho-(1'-*rac*-glycerol)), DMPC (1,2-dimyritoyl-*sn*-glycero-3-phosphocholine, cholesterol, DPC (n-dodecylphosphocholine), deuterated DPC, DHPC (1,2-dihexanoyl-*sn*-glycero-3-phosphocholine) (Avanti Polar Lipids); OG (n-Octyl-β-D-Glucopyranoside (Affymetrix); monoolein (1-Oleoyl-*rac*-glycerol), K^+ ionophore valinomycin, protonophore CCCP (carbonyl cyanide m-chlorophenyl hydrazone), Zn^{2+} ionophore (2-Mercaptopyridine *N*-oxide) (Sigma-Aldrich); fluorescent dyes FluoZin-3, Fluo-4 and HPTS, and fluorescent quencher DPX (Invitrogen).

IV. Analytical Ultracentrifugation (AUC)

Rocker peptide was dissolved in 10 mM DPC in predetermined density-matched buffer (10 mM HEPES, 50 mM KCl, 200μM EDTA in 60% D_2O, uncorrected pH 7.0) at the monomeric peptide concentrations of 60 μM, 100 μM or 140 μM in presence or absence of 500 μM $ZnSO_4$. The sedimentation equilibrium data were collected from the resulting samples with peptide monomer : detergent molar ratios of 0.6:1000, 1:100 and 1.4:1000 in presence or absence of Zn^{2+} at an initial concentration of 300 μM by radially scanning the absorbance at the wavelength of 280 nm upon reaching equilibrium at a total of five speed intervals ranging from 25,000 to 45,000 rpm at 25°C by using Beckman Optima XL-I analytical ultracentrifugation system.

In analyzing the sedimentation profiles, the peptide monomer molecular mass and partial specific volume, corrected for partial deuteration, were calculated using the modified version of SEDENTRP (*51, 52*). A single-species model initially used to fit the sedimentation profiles for the sample with excess Zn^{2+} provided a molecular weight of the sedimenting species that was slightly larger than the tetrameric molecular weight for deuterated Rocker. A model for fully cooperative dimer-tetramer-octomer equilibrium provided an excellent simultaneous fit. This model is plausible also because the dimeric crystal structures in different condition indicate high biophysical stability of the tight dimer. The octamer in the model may indicate multiple tetramers encapsulated in a micelle.

V. X-Ray Crystallography

Tetragonal crystals in the space group of $P4_32_12$ were obtained by vapor diffusion of hanging drops consisting 1:1 (vol.) mixture of OG-bound Rocker with a para-bromo-phenylalanine at position 2 (Rocker Br-Phe2) (1 mM peptide, 2 mM $ZnSO_4$, 50 mM OG) and the well solution (20 mM Li_2SO_4, 50 mM sodium citrate (pH 5.6), 21 % (w/v) PEG1000), inverted above the well solution and incubated at room temperature over two weeks. Tetragonal crystals in the space group of $I4_122$ were obtained, via lipidic cubic phase (LCP) method, from 100 nl boluses containing monoolein-bound Rocker Br-Phe2 (4 mM peptide, 60% (vol) monoolein, 6 mM $ZnSO_4$) immersed in 1 μl of precipitation buffer (0.05 M Li_2SO_4, 0.1 M tricine (pH 7.4), 7 % (w/v) PEG 3000) incubated in 0.1-mm-deep wells at room temperature over a month. Cubic crystals in the space group of $I2_13$ were obtained via vapor diffusion of hanging drops consisting 1:1 (vol.) mixture of OG-bound Rocker (1 mM peptide, 1 mM $CoSO_4$, 50 mM OG) and the well solution (360 mM LiCl, 100 mM sodium citrate (pH 5.6), 28 % (w/v) PEG 400, 1.56M 1,2-hexanedediol) inverted above the well solution and incubated at room temperature over 2.5 weeks.

Crystals were flash frozen without additional cryoprotectant and stored in liquid nitrogen. Data from the crystals obtained from hanging drops and LCP were collected under a cold stream of nitrogen using the Advanced Light Source beam line 8.3.1 at the Lawrence-Berkeley National Laboratory and the Advanced Photon Source beam line 24-ID-C at the Argonne National Laboratory, respectively.

The diffraction data from primitive tetragonal and cubic crystals were reduced by using MOSFLM and scaled by SCALA (*53*); and the data from I-centered tetragonal crystal were processed by using the HKL2000 package (*54*).

Molecular replacement strategy coded/implemented in PHASER (*55*) was sought for phasing the $P4_32_12$ dataset using a poly-alanine alpha helix of 25 residues as a probe**.** Dimer in the asymmetric unit suggested by the Matthews coefficient (V_m= 2.35 $Å^3$/Da) was located by

searching the second helix around a pre-located first helix in initial molecular replacement solution. The dimer solution obtained had the scores LLG=150, TFZ =8.6; CC=0.75 and R_{work}/R_{free} =0.397/0.423. To the MR solution, residues 23-25 at C-termini were truncated to have helices of equal length. The rigid body refinement followed by iterative model building and restrained refinements adopted in *Auto Build* module of PHENIX package (*56*) was used on the MR model. All residues were traced in the electron density map, during which model statistics were R_{work}/R_{free}=0.316/0.345.

For the $I4_122$ dataset, the monomer suggested by the Matthews coefficient (V_M = 2.82 Å/Da) was located with a use of an idealized 25-residue-long poly-alanine α-helix as a probe by using PHASER. Structures were refined by using the PHENIX package. The refined monomeric solution for the $I4_122$ data formed the expected tight dimer with its symmetry mate.

The Matthews coefficient (V_m= 2.35$Å^3$/Da) for the $I2_13$ suggested a tetramer in the asymmetric unit. The MR phasing using *PHASER* MR protocol could locate only a dimer in the asymmetric unit with model statistics of CC=0.60 and R_{work}/R_{free}=0.489/0.530.

Five to ten per cent of the reflections were withheld for the calculation of R_{free}. See **Table S5** for detailed data collection and refinement statics.

Table S5. X-ray data collection and refinement statistics.

PDB ID	4P6J	4P6K	4P6L
Protein/Environment	Rocker *p*-Br-Phe2/Octyl Glucoside	Rocker *p*-Br-Phe2/ Monoolein LCP	Rocker/Octyl Glucoside
Data Collection			
Wavelength (Å)	0.91996	0.9198	1.1159
Space Group	P 4_3 2_1 2	I 4_1 2 2	I 2_1 3
Cell Dimensions			
a, b, c (Å)	41.45, 41.45, 63.99	46.87, 46.87, 60.60	87.12, 87.12, 87.12
α, β, γ (°)	90	90	90
Resolution (Å)	50-2.80 (2.95-2.80)	50-2.70 (2.80-2.70)	61.10-2.80 (2.95-2.80)
R_{sym}	0.099 (0.549)	0.117 (0.628)	0.055 (0.750)
I / σI	10.6 (3.2)	15.2 (2.0)	13.5 (1.7)
Completeness (%)	100 (100)	89.4 (86.7)	95.5 (100)
Redundancy	6.2 (6.6)	10.8 (9.8)	6.3 (4.5)
Refinement			
Resolution (Å)	34.79-2.80	37.08-2.70	43.56-2.80
# of Reflections Used	2615	1601	2598
R_{work} / R_{free}	0.248/0.272	0.295/0.305	0.292/0.303
# of Atoms			
Protein	422	211	422
Water	0	0	0
Ligand	5		
B-factor			
Protein	46.3	70.0	96.7
Water			
Ligand	89.2		
r.m.s. Deviation			
Bond Length (Å)	0.002	0.003	0.002
Bond Angles (°)	0.452	0.386	0.399
Ramachandran Statistics (%)			
Core	97.8	95.2	97.8
Allowed Region	2.2	4.8	2.2
Disallowed Region	0	0	0

Values in the parentheses are for the highest resolution range.

VI. Liposome Flux Assay

Rocker or its variants were reconstituted in large unilamellar vesicles (LUVs) consisting POPC, POPG and cholesterol mixed at a molar ratio of 4:1:2, with a peptide:lipid ratio (not counting cholesterol) of 1:1000 or 1.32:2000 by using the extrusion method (*57*). Briefly, organic solvent was removed from the mixture of lipid and peptide under N_2 then under at least 4 hours of lyophilization to form dry film. The film was re-suspended in the interior buffer to achieve the lipid concentration of 25 mM, followed by ten cycles of freeze-thaw-vortex. The resuspension was extruded 11 times across 100-nm sizing membrane. The buffer to the vesicle exterior was exchanged by washing the resulting LUVs using 0.5 ml Zeba 40k MWC size-exclusion spin column (Thermo Scientific) preconditioned in desired exterior buffer or by two cycles of dialysis at 4°C overnight.

To quantify washed or dialyzed proteoliposomes, LC-MS was used to determine the ion count for POPC from an aliquot of proteoliposome. The ion count was calibrated with a predetermined amount of deuterated POPC (16:0-D31-18:1 PC, Avanti Polar Lipids) included as an internal standard. Proteoliposomes were then appropriately diluted in exterior buffer to achieve the final lipid concentration of 800 μM and kept at 18°C to be used for experiments on the same day.

To measure Zn^{2+} or Ca^{2+} efflux, both interior and exterior buffers were prepared to contain 100 μM of $ZnSO_4$ or $CaSO_4$, while the assay buffer contained 10 mM EDTA. To set up metal-ion influx assays, the interior and exterior buffers were free of divalent metal cation, while the assay buffer contained varying concentrations of $ZnSO_4$ or $CoSO_4$. The interior buffers contained 200 μM FluoZin-3, 750 μM calcein, 750 μM Fluo-4 or 500 μM HPTS for monitoring Zn^{2+}, Co^{2+}, Ca^{2+} or proton, respectively. The exterior buffer was identical to the respective interior buffer, except the exterior buffer did not contain the fluorescent dye. The assay buffer contained 20 mM DPX. A given set of interior, exterior and assay buffers for a corresponding assay was prepared to contain 5 mM MOPSO, pH 6.8 or 7.0, with an electrolyte consisting 50 mM K_2SO_4, 50 mM Na_2SO_4, or 80 mM *N*-methyl-D-glucamine.

Ion flux was generally measured under single-turnover conditions, and initial rates were evaluated prior to buildup of an electrical potential. The change in the intravesicular ion concentration was monitored by detecting the fluorescence of preloaded membrane-impermeable dye by using the KinetAsyst Stopped-Flow system (TgK Scientific) at 18°C. Equal volumes of the proteoliposome sample and assay buffer were loaded into two separate mixing syringes, and ion flux was initiated by instantaneously injecting 75 μl of each reactants through the mixing cell simultaneously. For monitoring Zn^{2+}, samples were excited at 494 nm, and the time course was recorded for emissions monitored at 515 nm using a 10-nm bandpass filter. Zn^{2+} increases the fluorescence of FluoZin-3 complexometrically. For monitoring Co^{2+}, samples were excited at 496 nm, and the time course was recorded for emissions detected at 520 nm using a 10-nm bandpass filter. Co^{2+} quenches the fluorescence of calcein complexometrically. For monitoring proton, samples were excited alternately at 455 nm and 416 nm, and emissions were recorded at 520 nm using a 500-nm long-wave pass filter. The ratio of emission intensities at two excitation wavelengths (F_{455}/F_{416}) was calculated.

A standard curve was each generated for encapsulated FluoZin-3, Fluo-4 and HPTS, and free calcein. Proteoliposomes preloaded with FluoZin-3 or Fluo-4 was mixed, at a 1:1 ratio, with assay buffers containing varying concentrations of $ZnSO_4$ or $CaSO_4$ with corresponding metal ionophore at 800 nM and 800 nM CCCP, in the Stopped-Flow and allowed the intravesicular divalent metal concentration to equilibrate with the exterior divalent metal concentration over 25

minutes. The resulting fluorescence was plotted as a function of divalent metal concentrations. For pH calibration, LUVs preloaded with HPTS was prepared using K^+-containing buffers. Aliquots of LUVs were incubated with equal volumes of assay buffers containing 800 nM CCCP and 800 nM valinomycin with varying pHs for 30 minutes to allow the interior and exterior pHs to equilibrate. The emission spectra of each sample were determined at above two excitation wavelengths by using the TEACAN infinite M1000 plate reader; and pHs, by the Thermo Orion pH meter equipped with a Pinnacle semi-micro pH electrode. To generate HPTS/pH calibration, the ratio of integrals of emission spectra at the two excitations (F_{455}/F_{416}) was plotted against the corresponding pH values. For cobalt standard curve, the fluorescence of 750 μM Calcein in MOPSO/NMG buffer containing varying concentrations of Co^{2+} was measured with excitation at 496 nm and emission at 520 nm using TEACAN plate reader.

To quantitatively analyze the data for flux of divalent metal cation, the total interior concentration of metal, [metal], was determined from the normalized fluorescence of FluoZin-3, Fluo-4 or calcein, $\Delta F/\Delta F_{max}$, by using $\Delta[\text{metal}] \approx a\Delta F/\Delta F_{max}$, where a is a converting factor determined from the standard curve (*40*). For data from vesicles containing HPTS, the interior proton concentration, $[H^+]$, was determined from F_{455}/F_{416} by using the function, $[H^+] = 5.29(\frac{3.19}{F_{455}/F_{416}} - 1)$, obtained by non-linear curve fitting to describe the plots obtained for the HPTS/pH calibration.

The time-courses for the concentration of intravesicular Zn^{2+}, Co^{2+}, or H^+, [ion], were fit to a single exponential function combined with linear process, $[\text{ion}] = N_0 \exp(-k \times t) + mt + b$, where t is time, N_0 is the initial quantity, and k is the rate constant; and m and b are, respectively, the slope and [ion] at $t = 0$ for the linear component. The initial rate of transport, $V_i = \Delta[\text{ion}]/\Delta t_{(t\to 0)}$, was calculated as $-N_0 k + m$. Ions accumulated per tetrameric Rocker was calculated by assuming the surface area of 62.7 $Å^2$ occupied per a lipid molecule (not counting cholesterol) in 39.8-Å-thick bilayer (*58*) forming uniform vesicles with an outer diameter of 0.1 μm, as supported by dynamic light scattering and negative-stain electron microscopy (not shown). Dependence on the exterior ion concentration, $[\text{ion}]_{out}$, was analyzed by non-linear curve fitting of the initial transport rate in terms of ions accumulated per a tetrameric Rocker to a function under Michaelis-Menten model described by:

$$\frac{\text{ions accumulated per Rocker}}{\Delta t_{(t\to 0)}} = \frac{V_{max}[\text{ion}]_{out}}{K_M + [\text{ion}]_{out}}$$

Where V_{max} is the maximum initial transport rate per a tetrameric Rocker and K_M is the Michaelis-Menten constant.

VII. Solution NMR Experiments

The 1-Dimensional ^{1}H-NMR spectra of aromatic side-chains were monitored in increasing concentration of $ZnSO_4$ using deuterium-exchanged Rocker peptide reconstituted in deuterated DPC micelle. To exchange the backbone amide hydrogen atoms with deuterium, Rocker peptide prepared at the peptide monomer : detergent molar ratio of 1:100 in a D_2O buffer with 100 mM deuterated DPC and 10 mM HEPES pD 7.0 was incubated overnight, followed by lyophilization and re-suspension in equal volume of D_2O. The experiment was conducted on Bruker Biospin 900 MHz NMR spectrometer at 40°C.

VIII. Solid-state NMR experiments

Two isotopically labeled Rocker peptides (YYKEIAHALF SALFALSELY IAVRY) were synthesized, one containing para-^{19}F-lableled Phe14 and the other containing uniformly ^{13}C, ^{15}N-labeled Ile5, Ala8, Leu19 and Ala22. DMPC bilayers were used to reconstitute the peptides. The peptide: lipid molar ratio was 1 : 8 for all samples, corresponding to a mass ratio of ~1:2. To investigate the effect of Zn^{2+} binding on the peptide, we prepared two samples with and without $ZnSO_4$ in the DMPC vesicle solution. The apo and Zn^{2+} bound samples were prepared in 10 mM phosphate buffer and 10 mM MOPSO buffer, respectively. The MOPSO buffer was chosen for the bound sample to avoid the formation of the $Zn_3(PO_4)_2$ precipitate. The apo sample contains 1.8 mg peptide and the bound sample contains ~1.2 mg peptide. For the bound sample, the Zn^{2+}: peptide molar ratio is 4: 1, corresponding to a Zn^{2+}: tetramer ratio of 16: 1. The proteoliposome suspension was centrifuged at 55,000 rpm for 4 hours to give membrane pellets with ~40 wt% hydration. The ^{19}F-labeled Rocker/DMPC sample was packed into a 4 mm MAS rotor, while the ^{13}C, ^{15}N-labeled samples were packed into 2.5 mm MAS rotors for NMR experiments.

The ^{19}F CODEX experiments(*36*) were carried out on a Bruker DSX-400 MHz (9.4 Tesla) spectrometer with resonance frequencies of 400.5 MHz for ^{1}H and 376.8 MHz for ^{19}F. The experiments were conducted at 220 K under 8 kHz MAS using a 4 mm H/F/X probe. Typical radiofrequency field strengths were 71 kHz for ^{1}H and 50 kHz for ^{19}F. ^{19}F chemical shift was referenced to the ^{19}F signal of Teflon at -122.0 ppm. The peptide was immobilized at this low temperature, allowing us to detect spin diffusion effects to probe peptide oligomerization (*37, 59*). Two trains of ^{19}F π-pulses placed every half a rotor period were applied before and after the first mixing time to recouple the ^{19}F chemical shift anisotropy under MAS. To correct for ^{19}F T_1 relaxation effects, a z-filter was applied after the second π-pulse train. The CODEX experiments were conducted with a control (S_0) and a dephasing (S) experiment, and the normalized intensities, S/S_0, were measured as a function of the mixing time, which ranged from 0.05 s to 3 s, and were fit using a MATLAB program that takes into account all inter-^{19}F distances in the four-spin system (*60, 61*).

The ^{13}C, ^{15}N-labeled peptide samples were measured on a Bruker Avance II 600 MHz spectrometer (14.1 Tesla) using a 2.5 mm triple-resonance MAS probe. Typical radiofrequency field strengths were 100 kHz for ^{1}H decoupling, 62.5 kHz for ^{13}C and 41.7 kHz for ^{15}N. ^{13}C chemical shift was externally referenced to the Met ^{13}Cδ signal at 14.0 ppm of f-MLF-OH on the TMS scale, while ^{15}N chemical shift was referenced to the Phe ^{15}N signal at 110.1 ppm of formyl-MLF-OH on the liquid ammonia scale. ^{13}C CP spectra were measured under 11 kHz MAS from 233 K to 313 K. 2D ^{13}C-^{13}C and ^{15}N-^{13}C correlation spectra were measured at 233 K under 11 kHz MAS. The 2D ^{13}C-^{13}C correlation experiments were measured with and without DARR (*62*) irradiation for 30 ms and 500 ms, respectively. 2D ^{15}N-^{13}C correlation experiments utilized REDOR (*63*) for ^{15}N-^{13}C coherence transfer. ^{13}C-^{1}H dipolar couplings for probing peptide dynamics were measured using the 2D dipolar-chemical-shift (DIPSHIFT) correlation experiment (*64, 65*) at 303 K under 7 kHz MAS. ^{1}H homonuclear decoupling was achieved using the FSLG sequence (*66*) with a scaling factor of 0.577. The apparent dipolar couplings were obtained by fitting the t_1-domain of the DIPSHIFT time curve and dividing the coupling by the theoretical scaling factor 0.577. The resulting couplings were divided by the rigid-limit value of 22.7 kHz to obtain the order parameter S_{CH}. Experiments on the model peptide formyl-MLF-OH confirmed that the actual scaling factor does not deviate from the theoretical value of 0.577 within experimental uncertainty.

The insertion depth of the Rocker peptide in DMPC bilayers was measured using the 2D ^{13}C-detected ^{1}H spin diffusion experiment at 275 K under 7 kHz MAS. ^{1}H magnetization of water and lipids were selected by a ^{1}H T_2 filter and then transferred to the peptide through ^{1}H spin diffusion (*38*). This experiment is normally conducted near ambient temperature where water and lipids are both highly mobile and thus easily distinguishable from the peptide (*67*). However, the low intensities of the Rocker peptide at ambient temperature compelled us to use the moderate low temperature of 275 K to observe sufficiently high peptide signals. Fortunately, not only is water still mobile at 275 K, but the lipid chains are still sufficiently mobile to survive the T_2 filter of 0.4 ms to be selected.

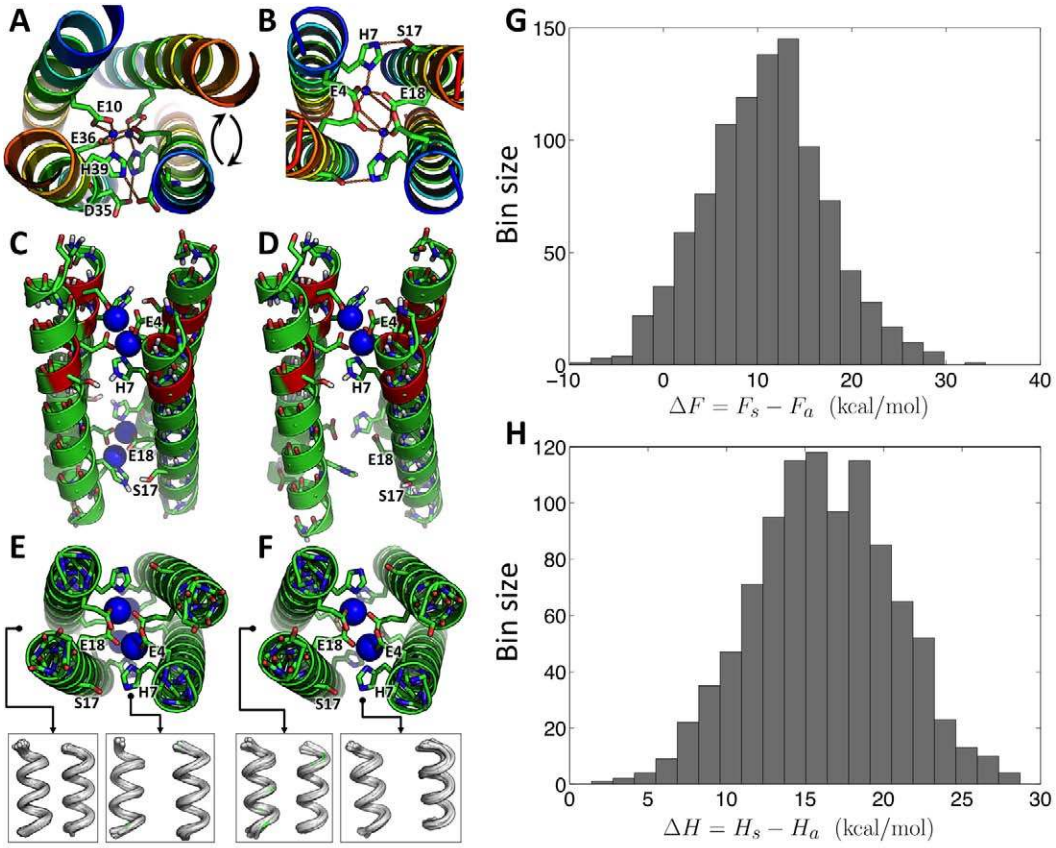

Fig. S1 Building templates for design. **A**, The metal binding geometry in a dimanganese four-helix bundle (PDB code 1LT1). **B**, The binding site considered here, with a topology equivalent to swapping metal coordinating residues between two adjacent chains of 1LT1, shown with black arrows in **A**. **C**, The final optimized symmetric template. The asymmetric template in **D** is created from the symmetric one by aligning ideal helices to the regions shown in red. The top row of **E** and **F** shows an axial view of the symmetric and asymmetric templates, respectively, revealing a narrow and a wide interface in each. The bottom row shows close structural matches (within a Cα RMSD of 0.6 or 0.7 A) from a non-redundant subset of the PDB to both interfacial geometries found by MaDCaT, indicating "designable" templates. Template interfaces are rendered in green, but are generally occluded by other structural matches. **G**, VALOCIDY-estimated thermodynamic parameters for sequences optimized in the protein design stage. **G** and **H** show the distributions of differences in free energy and enthalpy, respectively, between the symmetric and asymmetric states. Most sequences prefer the symmetric state and all prefer it enthalpically.

.

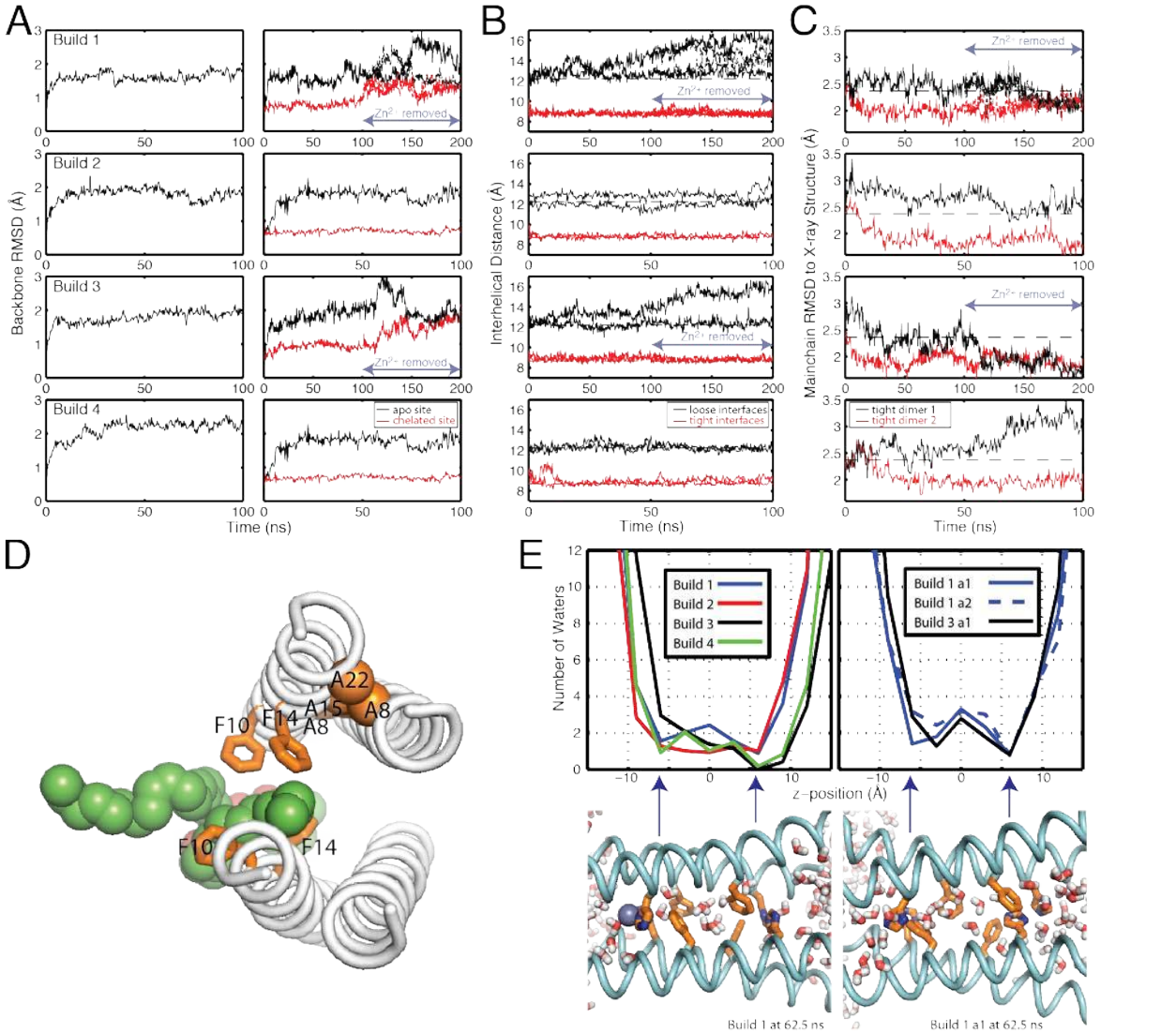

Fig. S2. MD to assess the stability and functionality of Rocker. A-C, The MD simulation of four different charge-states of Rocker, Build 1-4. Extended simulations were performed for Build 1 and 3 after removing di-Zn^{2+} at 100 ns. For Build 1, the simulation performed after removing Zn^{2+} was done in duplicate, and the second set of time courses is reported in dashed trace lines in the corresponding panels. **A**, The simulations are compared to the design model, which was used as the starting structure, and the Cα RMSDs to the starting structure are plotted for the protein chain (left panels) and the metal-binding residues (right panels) at the chelated zinc site (red traces) and metal-free zinc site (blue traces). **B**, The interhelical distances at the tight and loose interfaces of the simulated Rocker are plotted. **C**, Each of two tight dimers from individual simulations is compared to the LCP crystal structure. **D**, Snapshot of MD simulation for build 3 at 97 ns after the removal of Zn^{2+} shows the lipid acyl chain inserting into the loose interface of Rocker. **E**, Distribution of water molecules in the lumen throughout the simulations with di-Zn^{2+} (spheres) bound (left) or removed (right) is plotted as a function of the distance from the hydrocarbon center (top panels), with representative snapshots (bottom panels) aligned along the z-distance roughly to the scale. Bulky Phe14 coinciding with the dry zone (arrows) and the metal site His7 are in orange.

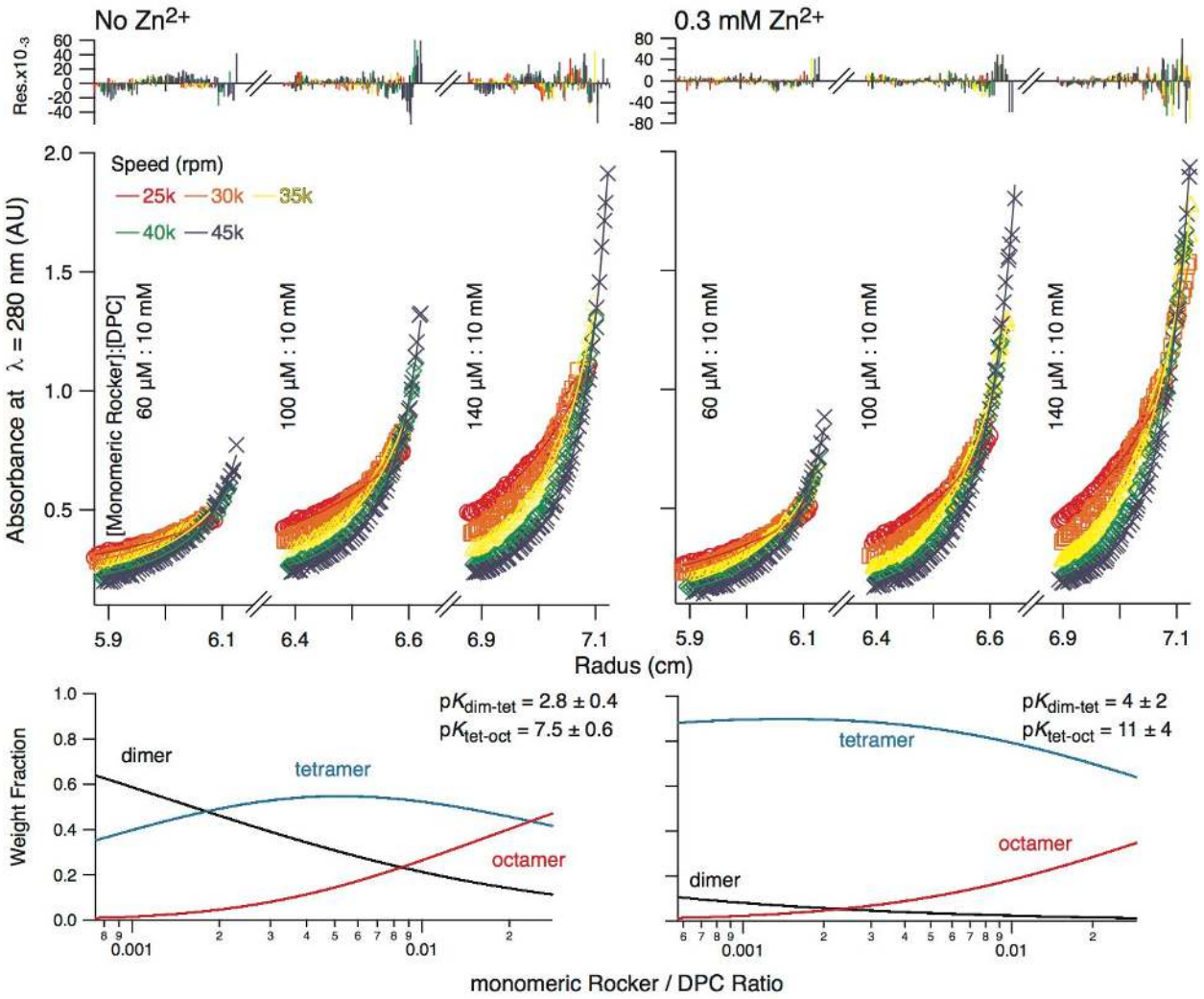

Fig. S3. Tetramerization of Rocker in DPC micelle in presence or absence of excess Zn^{2+} by density matched AUC. Sedimentation profiles (middle panels) of varying concentrations of peptide in density-matched DPC detergent at five different radial velocities in presence or absence of excess Zn^{2+} (right and left, respectively) were globally in satisfactory agreement with fully cooperative dimer-tetramer-octamer equilibrium, as indicated by the low residuals from fittings (upper panels). $pK_{Association}$ values determined from the global fit for dimer-tetramer and tetramer-octamer equilibria are 2.8 ± 0.4 and 7.5 ± 0.6 in absence of Zn^{2+}, and 4 ± 2 and 11 ± 4 in presence of excess Zn^{2+}, respectively, with the error values indicating SDs propagated from curve fitting. The resulting expected population of each species over varying peptide:detergent ratios are respectively plotted on the lower panels.

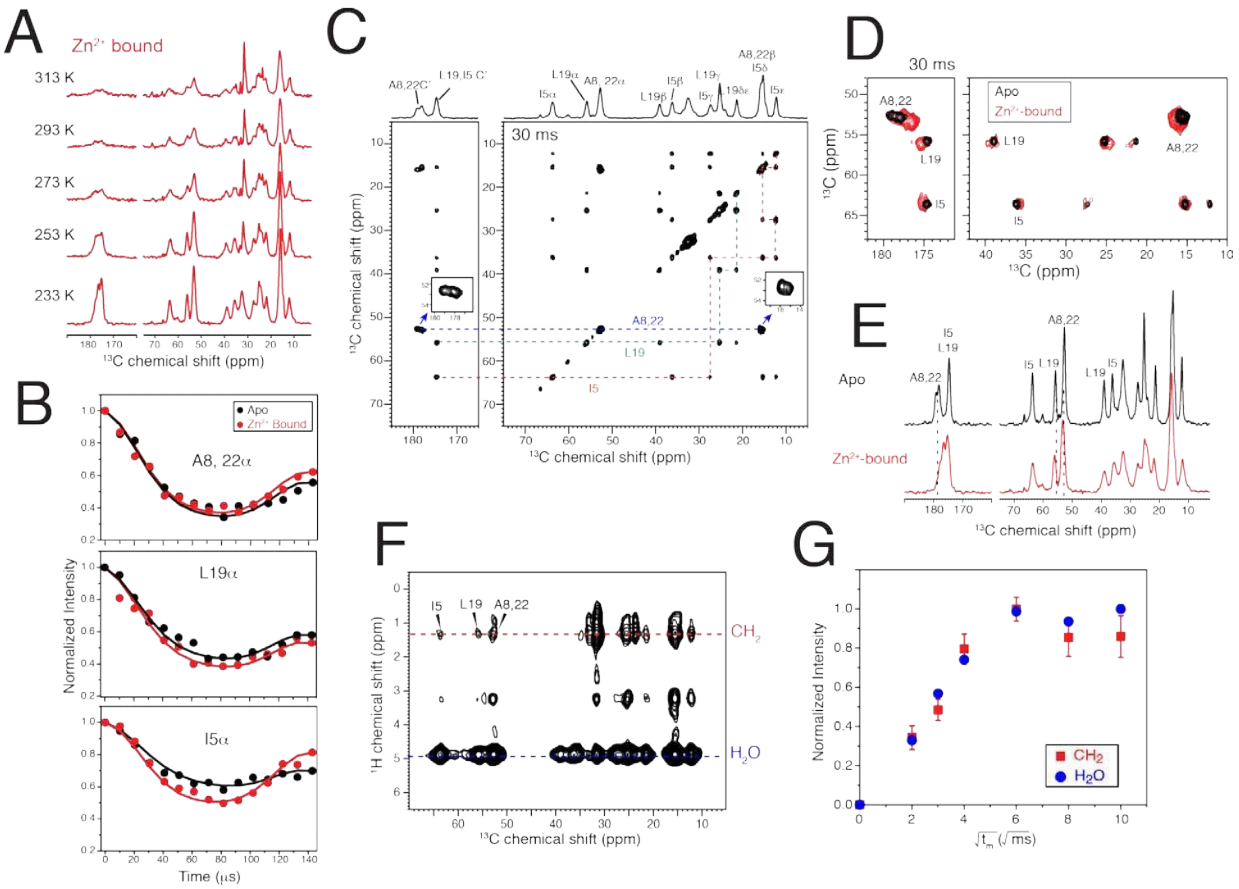

Fig. S4. Structure and dynamics of the Rocker peptide in DMPC bilayers with and without Zn^{2+}. A, 1D ^{13}C CP-MAS spectra of Zn^{2+} bound peptide from 233 K to 313 K. The peptide exhibits intermediate-timescale conformational motion at high temperature, similar to the apo peptide. **B**, ^{13}C-^{1}H dipolar couplings of the A8/A22, L19 and I5 Cα signals of apo and Zn^{2+}-bound Rocker in DMPC bilayers at 303 K on top, middle and bottom panels, respectively. The couplings fit to order parameter, S_{CH}, of 0.84 for A8/22Cα of both apo and Zn^{2+}-bound states, 0.73 and 0.77 for L19Cα of the apo and bound states, and 0.55 and 0.75 for I5Cα of the apo and bound states, respectively, but the intensities decay at the end of the rotor period, indicating the globally present microsecond-timescale motion. **C**, 2D ^{13}C-^{13}C DARR correlation spectrum of the apo peptide at 30 ms mixing at 233 K. The spectral resolution is sufficiently high to partly resolve the A8 and A22 signals. **D**, Overlay of the 2D ^{13}C-^{13}C correlation spectra of apo (black) and Zn^{2+} bound (red) Rocker peptides, showing that the most significant chemical shift changes occur at A8/A22. **E**, Comparison of the 1D ^{13}C spectra of apo and Zn^{2+} bound Rocker at 233 K. **F**, Representative 2D ^{13}C-detected ^{1}H spin diffusion spectra of the apo peptide at a mixing time of 36 ms. Clear lipid CH_2 – peptide cross peaks are observed. The spectrum was measured at 275 K. **G**, ^{1}H spin diffusion buildup curves from water and lipid chains to the peptide for the apo Rocker. The fast buildup of the lipid – peptide cross peaks indicate that the peptide is well inserted into the DMPC bilayer. Error bars are SD propagated from signal-to-noise.

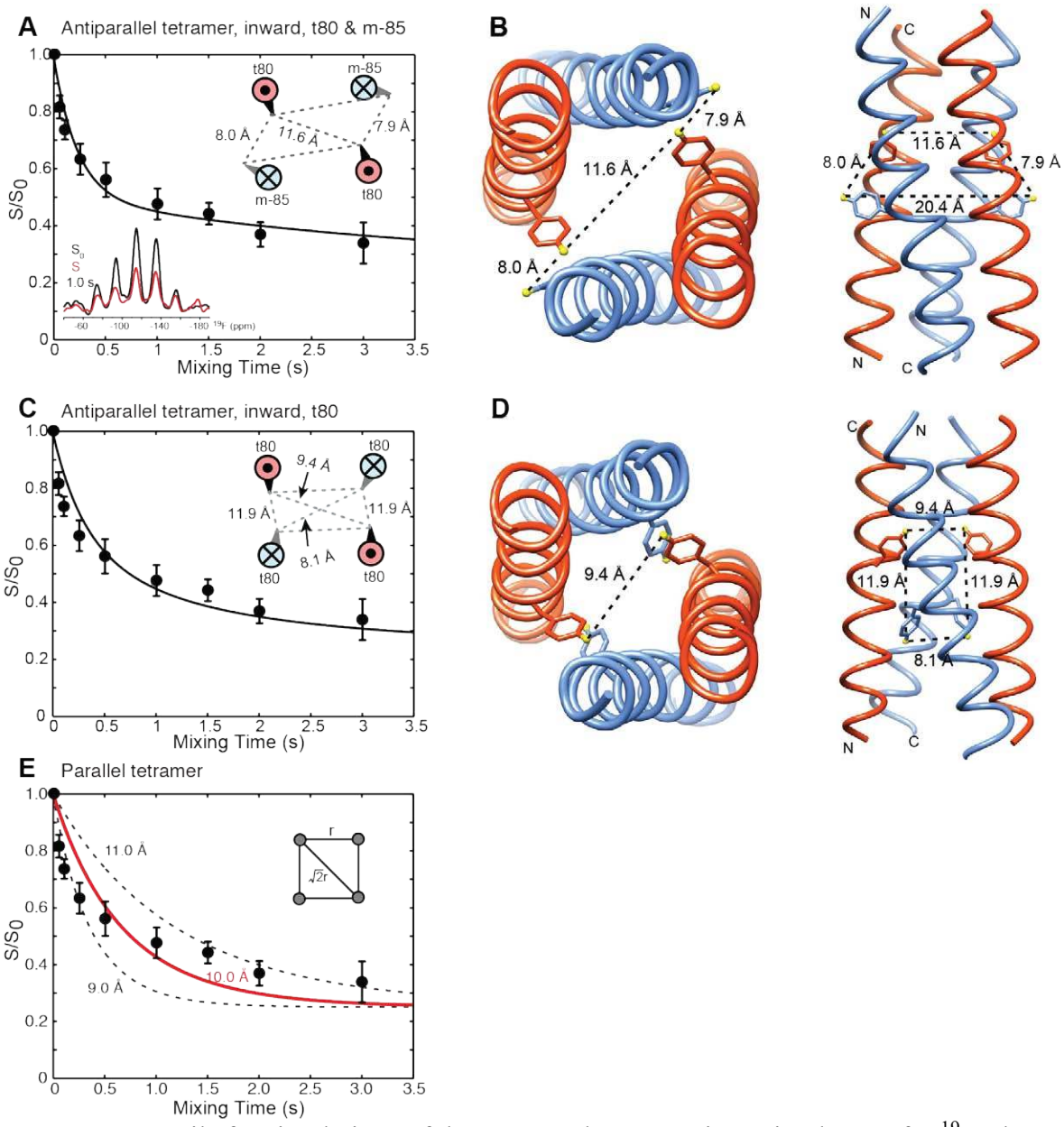

Figure S5. Details for simulations of the measured CODEX intensity decay of 4-^{19}F-Phe14-labeled Rocker bound to DMPC bilayers shown in Fig. 3D. **A**, Simulations using an antiparallel tetramer structural model with inward-facing Phe14 residues, assuming Phe rotamers of t80 and m-85. The shortest ^{19}F-^{19}F distance within the non-planar quadrilateral is ~8.0 Å. **B**, Top and side view of the tetramer structure, with t80 for the red helices and m-85 for the blue helices. The shortest distances of 8.0 Å are found between two oppositely oriented helices and are roughly along the bundle axis. **C**, Simulations using an antiparallel tetramer structural model with inward-facing Phe14 residues, using the t80 rotamer for all four Phe14. The shortest ^{19}F-^{19}F distance is 8.1 Å. **D**, Top and side views of this tetramer model. The shortest ^{19}F-^{19}F distance of 8.1 Å is found between two parallel oriented helices, roughly transverse to the bundle axis. **E**, Simulations using a hypothetical parallel tetramer model with a square geometry for the four ^{19}F atoms. The best-effort fit using a ^{19}F-^{19}F distance of 10 Å still fails to reproduce the bi-exponential nature of the measured intensity decay.

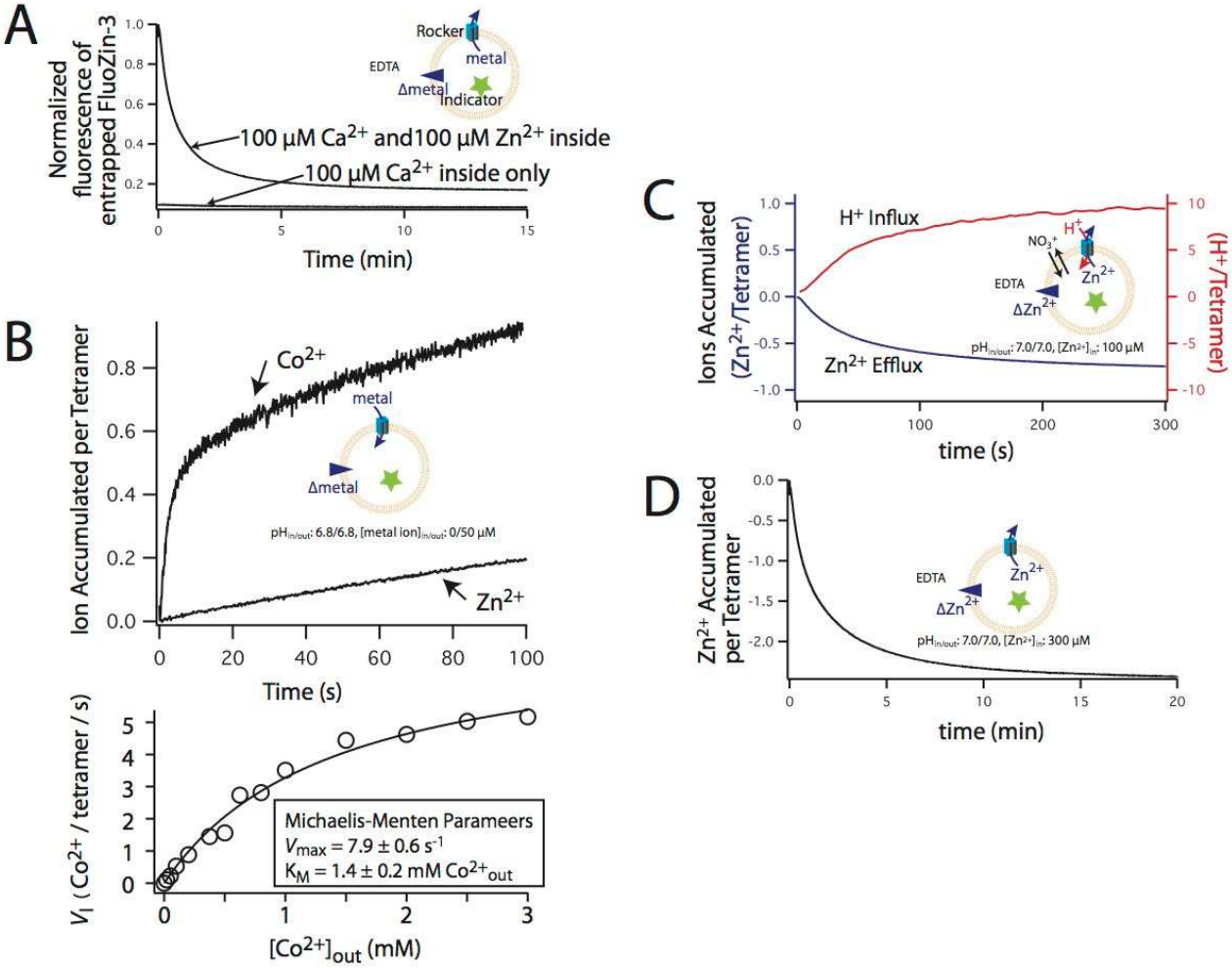

Fig. S6. Liposome flux assay controls. A, LUV reconstituted with Rocker is preloaded with Zn^{2+}-specific dye FluoZin-3. Adding EDTA to the exterior of Ca^{2+}-filled proteoliposome results in insignificant change in negligible fluorescence. So, the change in fluorescence for LUV co-loaded with Zn^{2+} and Ca^{2+} is due to efflux of Zn^{2+}, indicating absence of affinity for Ca^{2+} by the di-Zn^{2+}-site. **B**, Co^{2+} is imported at a faster rate than Zn^{2+} (top), consistent with weaker binding of Co^{2+} to the metal-site expected from the Irving-Williams series. The initial rate of Co^{2+} transport, V_i, increases hyperbolically with exterior Co^{2+}, following Michaelis-Menten kinetics, with V_{max} of 7.9 ± 0.6 ions/tetramer/s and K_M of 1.4 ± 0.2 mM $Co^{2+}{}_{out}$ (bottom). Significantly larger K_M and V_{max} for Co^{2+} transport than Zn^{2+} is consistent with lower affinity of Co^{2+}. Error values are SD propagated from curve fitting. **C**, In the absence of electrical charge provided by membrane-permeable NO_3^+, Zn^{2+} gradient created by exterior EDTA still drives proton influx, indicating obligatory antiport. **A** and **C** are done at 20°C with pH of 7 inside and out; **B** is done at 18°C with pH of 6.8 inside and out. **D,** Multiple turnovers of Zn^{2+} transport through Rocker.

References and Notes

1. N. Koga, R. Tatsumi-Koga, G. Liu, R. Xiao, T. B. Acton, G. T. Montelione, D. Baker, Principles for designing ideal protein structures. *Nature* **491**, 222–227 (2012). Medline doi:10.1038/nature11600

2. M. L. Zastrow, V. L. Pecoraro, Designing functional metalloproteins: From structural to catalytic metal sites. *Coord. Chem. Rev.* **257**, 2565–2588 (2013). Medline doi:10.1016/j.ccr.2013.02.007

3. C. E. Tinberg, S. D. Khare, J. Dou, L. Doyle, J. W. Nelson, A. Schena, W. Jankowski, C. G. Kalodimos, K. Johnsson, B. L. Stoddard, D. Baker, Computational design of ligand-binding proteins with high affinity and selectivity. *Nature* **501**, 212–216 (2013). Medline doi:10.1038/nature12443

4. A. J. Reig, M. M. Pires, R. A. Snyder, Y. Wu, H. Jo, D. W. Kulp, S. E. Butch, J. R. Calhoun, T. Szyperski, E. I. Solomon, W. F. DeGrado, Alteration of the oxygen-dependent reactivity of de novo Due Ferri proteins. *Nat. Chem.* **4**, 900–906 (2012). Medline doi:10.1038/nchem.1454

5. M. L. Zastrow, A. F. A. Peacock, J. A. Stuckey, V. L. Pecoraro, Hydrolytic catalysis and structural stabilization in a designed metalloprotein. *Nat. Chem.* **4**, 118–123 (2012). Medline doi:10.1038/nchem.1201

6. M. L. Zastrow, V. L. Pecoraro, Influence of active site location on catalytic activity in de novo-designed zinc metalloenzymes. *J. Am. Chem. Soc.* **135**, 5895–5903 (2013). Medline doi:10.1021/ja401537t

7. G. Kiss, N. Çelebi-Ölçüm, R. Moretti, D. Baker, K. N. Houk, Computational enzyme design. *Angew. Chem. Int. Ed. Engl.* **52**, 5700–5725 (2013). 10.1002/anie.201204077 Medline doi:10.1002/anie.201204077

8. I. V. Korendovych, A. Senes, Y. H. Kim, J. D. Lear, H. C. Fry, M. J. Therien, J. K. Blasie, F. A. Walker, W. F. Degrado, De novo design and molecular assembly of a transmembrane diporphyrin-binding protein complex. *J. Am. Chem. Soc.* **132**, 15516–15518 (2010). Medline doi:10.1021/ja107487b

9. J. M. Perez-Aguilar, J. G. Saven, Computational design of membrane proteins. *Structure* **20**, 5–14 (2012). Medline doi:10.1016/j.str.2011.12.003

10. S. Radestock, L. R. Forrest, The alternating-access mechanism of MFS transporters arises from inverted-topology repeats. *J. Mol. Biol.* **407**, 698–715 (2011). Medline doi:10.1016/j.jmb.2011.02.008

11. O. Jardetzky, Simple allosteric model for membrane pumps. *Nature* **211**, 969–970 (1966). Medline doi:10.1038/211969a0

12. P. Mitchell, A general theory of membrane transport from studies of bacteria. *Nature* **180**, 134–136 (1957). Medline doi:10.1038/180134a0

13. E. A. Morrison, G. T. DeKoster, S. Dutta, R. Vafabakhsh, M. W. Clarkson, A. Bahl, D. Kern, T. Ha, K. A. Henzler-Wildman, Antiparallel EmrE exports drugs by exchanging between asymmetric structures. *Nature* **481**, 45–50 (2012). Medline doi:10.1038/nature10703

14. W. F. DeGrado, Z. R. Wasserman, J. D. Lear, Protein design, a minimalist approach. *Science* **243**, 622–628 (1989). Medline doi:10.1126/science.2464850

15. J. D. Lear, Z. R. Wasserman, W. F. DeGrado, Synthetic amphiphilic peptide models for protein ion channels. *Science* **240**, 1177–1181 (1988). Medline doi:10.1126/science.2453923

16. M. Hong, W. F. DeGrado, Structural basis for proton conduction and inhibition by the influenza M2 protein. *Protein Sci.* **21**, 1620–1633 (2012). Medline doi:10.1002/pro.2158

17. A. Pasternak, J. Kaplan, J. D. Lear, W. F. Degrado, Proton and metal ion-dependent assembly of a model diiron protein. *Protein Sci.* **10**, 958–969 (2001). Medline doi:10.1110/ps.52101

18. F. H. C. Crick, The Fourier Transform of a Coiled-Coil. *Acta Crystallogr.* **6**, 685–689 (1953). doi:10.1107/S0365110X53001952

19. G. Grigoryan, W. F. Degrado, Probing designability via a generalized model of helical bundle geometry. *J. Mol. Biol.* **405**, 1079–1100 (2011). Medline doi:10.1016/j.jmb.2010.08.058

20. C. M. Summa, A. Lombardi, M. Lewis, W. F. DeGrado, Tertiary templates for the design of diiron proteins. *Curr. Opin. Struct. Biol.* **9**, 500–508 (1999). Medline doi:10.1016/S0959-440X(99)80071-2

21. A. Lombardi, C. M. Summa, S. Geremia, L. Randaccio, V. Pavone, W. F. DeGrado, Retrostructural analysis of metalloproteins: Application to the design of a minimal model for diiron proteins. *Proc. Natl. Acad. Sci. U.S.A.* **97**, 6298–6305 (2000). Medline doi:10.1073/pnas.97.12.6298

22. Y. Chao, D. Fu, Thermodynamic studies of the mechanism of metal binding to the *Escherichia coli* zinc transporter YiiP. *J. Biol. Chem.* **279**, 17173–17180 (2004). Medline doi:10.1074/jbc.M400208200

23. G. Grigoryan, A. W. Reinke, A. E. Keating, Design of protein-interaction specificity gives selective bZIP-binding peptides. *Nature* **458**, 859–864 (2009). Medline doi:10.1038/nature07885

24. G. Grigoryan, Absolute free energies of biomolecules from unperturbed ensembles. *J. Comput. Chem.* **34**, 2726–2741 (2013). Medline doi:10.1002/jcc.23448

25. T. Lazaridis, Effective energy function for proteins in lipid membranes. *Proteins* **52**, 176–192 (2003). Medline doi:10.1002/prot.10410

26. A. Senes, D. C. Chadi, P. B. Law, R. F. Walters, V. Nanda, W. F. Degrado, E(z), a depth-dependent potential for assessing the energies of insertion of amino acid side-chains into membranes: Derivation and applications to determining the orientation of transmembrane and interfacial helices. *J. Mol. Biol.* **366**, 436–448 (2007). Medline doi:10.1016/j.jmb.2006.09.020

27. C. A. Schramm, B. T. Hannigan, J. E. Donald, C. Keasar, J. G. Saven, W. F. Degrado, I. Samish, Knowledge-based potential for positioning membrane-associated structures and assessing residue-specific energetic contributions. *Structure* **20**, 924–935 (2012). Medline doi:10.1016/j.str.2012.03.016

28. C. M. Summa, M. M. Rosenblatt, J. K. Hong, J. D. Lear, W. F. DeGrado, Computational de novo design, and characterization of an A(2)B(2) diiron protein. *J. Mol. Biol.* **321**, 923–938 (2002). Medline doi:10.1016/S0022-2836(02)00589-2

29. Y. Zhang, D. W. Kulp, J. D. Lear, W. F. DeGrado, Experimental and computational evaluation of forces directing the association of transmembrane helices. *J. Am. Chem. Soc.* **131**, 11341–11343 (2009). Medline doi:10.1021/ja904625b

30. S. Unterreitmeier, A. Fuchs, T. Schäffler, R. G. Heym, D. Frishman, D. Langosch, Phenylalanine promotes interaction of transmembrane domains via GxxxG motifs. *J. Mol. Biol.* **374**, 705–718 (2007). Medline doi:10.1016/j.jmb.2007.09.056

31. D. T. Moore, B. W. Berger, W. F. DeGrado, Protein-protein interactions in the membrane: sequence, structural, and biological motifs. *Structure* **16**, 991–1001 (2008). Medline doi:10.1016/j.str.2008.05.007

32. L. Cristian, J. D. Lear, W. F. DeGrado, Use of thiol-disulfide equilibria to measure the energetics of assembly of transmembrane helices in phospholipid bilayers. *Proc. Natl. Acad. Sci. U.S.A.* **100**, 14772–14777 (2003). Medline doi:10.1073/pnas.2536751100

33. K. R. MacKenzie, K. G. Fleming, Association energetics of membrane spanning alpha-helices. *Curr. Opin. Struct. Biol.* **18**, 412–419 (2008). Medline doi:10.1016/j.sbi.2008.04.007

34. E. R. deAzevedo, K. Saalwachter, O. Pascui, A. A. de Souza, T. J. Bonagamba, D. Reichert, Intermediate motions as studied by solid-state separated local field NMR experiments. *J. Chem. Phys.* **128**, 104505 (2008). Medline doi:10.1063/1.2831798

35. M. F. Cobo, A. Achilles, D. Reichert, E. R. Deazevedo, K. Saalwächter, Recoupled separated-local-field experiments and applications to study intermediate-regime molecular motions. *J. Magn. Reson.* **221**, 85–96 (2012). Medline doi:10.1016/j.jmr.2012.05.003

36. E. R. deAzevedo, W.-G. Hu, T. J. Bonagamba, K. Schmidt-Rohr, Centerband-only detection of exchange: Efficient analysis of dynamics in solids by NMR. *J. Am. Chem. Soc.* **121**, 8411–8412 (1999). doi:10.1021/ja992022v

37. J. J. Buffy, A. J. Waring, M. Hong, Determination of peptide oligomerization in lipid bilayers using 19F spin diffusion NMR. *J. Am. Chem. Soc.* **127**, 4477–4483 (2005). Medline doi:10.1021/ja043621r

38. D. Huster, X. Yao, M. Hong, Membrane protein topology probed by (1)H spin diffusion from lipids using solid-state NMR spectroscopy. *J. Am. Chem. Soc.* **124**, 874–883 (2002). Medline doi:10.1021/ja017001r

39. M. Hong, Oligomeric structure, dynamics, and orientation of membrane proteins from solid-state NMR. *Structure* **14**, 1731–1740 (2006). Medline doi:10.1016/j.str.2006.10.002

40. Y. Chao, D. Fu, Kinetic study of the antiport mechanism of an *Escherichia coli* zinc transporter, ZitB. *J. Biol. Chem.* **279**, 12043–12050 (2004). Medline doi:10.1074/jbc.M313510200

41. R. J. P. W. H. Irving, R. J. P. Williams, The stability of transition-metal complexes. *J. Chem. Soc.* 3192–3210 (1953). doi:10.1039/jr9530003192

42. M. Rapp, E. Granseth, S. Seppälä, G. von Heijne, Identification and evolution of dual-topology membrane proteins. *Nat. Struct. Mol. Biol.* **13**, 112–116 (2006). Medline doi:10.1038/nsmb1057

43. W. F. DeGrado, L. Di Costanzo, S. Geremia, A. Lombardi, V. Pavone, L. Randaccio, Sliding helix and change of coordination geometry in a model di-MnII protein. *Angew. Chem. Int. Ed. Engl.* **42**, 417–420 (2003). Medline doi:10.1002/anie.200390127

44. J. Zhang, G. Grigoryan, Mining tertiary structural motifs for assessment of designability. *Methods Enzymol.* **523**, 21–40 (2013). Medline doi:10.1016/B978-0-12-394292-0.00002-3

45. S. C. Lovell, J. M. Word, J. S. Richardson, D. C. Richardson, The penultimate rotamer library. *Proteins* **40**, 389–408 (2000). Medline doi:10.1002/1097-0134(20000815)40:3<389::AID-PROT50>3.0.CO;2-2

46. M. A. Hallen, D. A. Keedy, B. R. Donald, Dead-end elimination with perturbations (DEEPer): A provable protein design algorithm with continuous sidechain and backbone flexibility. *Proteins* **81**, 18–39 (2013). Medline doi:10.1002/prot.24150

47. C. E. Chang, M. J. Potter, M. K. Gilson, Calculation of molecular configuration integrals. *J. Phys. Chem. B* **107**, 1048–1055 (2003). doi:10.1021/jp027149c

48. B. R. Brooks, C. L. Brooks 3rd, A. D. Mackerell Jr., L. Nilsson, R. J. Petrella, B. Roux, Y. Won, G. Archontis, C. Bartels, S. Boresch, A. Caflisch, L. Caves, Q. Cui, A. R. Dinner, M. Feig, S. Fischer, J. Gao, M. Hodoscek, W. Im, K. Kuczera, T. Lazaridis, J. Ma, V. Ovchinnikov, E. Paci, R. W. Pastor, C. B. Post, J. Z. Pu, M. Schaefer, B. Tidor, R. M. Venable, H. L. Woodcock, X. Wu, W. Yang, D. M. York, M. Karplus, CHARMM: The biomolecular simulation program. *J. Comput. Chem.* **30**, 1545–1614 (2009). Medline doi:10.1002/jcc.21287

49. R. H. Stote, M. Karplus, Zinc binding in proteins and solution: A simple but accurate nonbonded representation. *Proteins* **23**, 12–31 (1995). Medline doi:10.1002/prot.340230104

50. J. C. Phillips, R. Braun, W. Wang, J. Gumbart, E. Tajkhorshid, E. Villa, C. Chipot, R. D. Skeel, L. Kalé, K. Schulten, Scalable molecular dynamics with NAMD. *J. Comput. Chem.* **26**, 1781–1802 (2005). Medline doi:10.1002/jcc.20289

51. T. M. Laue, W. F. Stafford 3rd, Modern applications of analytical ultracentrifugation. *Annu. Rev. Biophys. Biomol. Struct.* **28**, 75–100 (1999). Medline doi:10.1146/annurev.biophys.28.1.75

52. D. P. Kharakoz, V. E. Bychkova, Molten globule of human alpha-lactalbumin: hydration, density, and compressibility of the interior. *Biochemistry* **36**, 1882–1890 (1997). Medline doi:10.1021/bi960264r

53. A. G. W. Leslie, H. R. Powell, Processing diffraction data with MOSFLM. *NATO Sci Ser II Math* **245**, 41–51 (2007). doi:10.1007/978-1-4020-6316-9_4

54. Z. Otwinowski, W. Minor, in *Macromolecular Crystallography, Pt A*. (Academic Press Inc, San Diego, 1997), vol. 276, pp. 307-326.

55. A. J. McCoy, R. W. Grosse-Kunstleve, P. D. Adams, M. D. Winn, L. C. Storoni, R. J. Read, Phaser crystallographic software. *J. Appl. Crystallogr.* **40**, 658–674 (2007). Medline doi:10.1107/S0021889807021206

56. P. D. Adams, P. V. Afonine, G. Bunkóczi, V. B. Chen, I. W. Davis, N. Echols, J. J. Headd, L. W. Hung, G. J. Kapral, R. W. Grosse-Kunstleve, A. J. McCoy, N. W. Moriarty, R. Oeffner, R. J. Read, D. C. Richardson, J. S. Richardson, T. C. Terwilliger, P. H. Zwart, PHENIX: A comprehensive Python-based system for macromolecular structure solution. *Acta Crystallogr. D Biol. Crystallogr.* **66**, 213–221 (2010). Medline doi:10.1107/S0907444909052925

57. C. Ma, A. L. Polishchuk, Y. Ohigashi, A. L. Stouffer, A. Schön, E. Magavern, X. Jing, J. D. Lear, E. Freire, R. A. Lamb, W. F. DeGrado, L. H. Pinto, Identification of the functional

core of the influenza A virus A/M2 proton-selective ion channel. *Proc. Natl. Acad. Sci. U.S.A.* **106**, 12283–12288 (2009). Medline doi:10.1073/pnas.0905726106

58. N. Kučerka, M. P. Nieh, J. Katsaras, Fluid phase lipid areas and bilayer thicknesses of commonly used phosphatidylcholines as a function of temperature. *Biochim. Biophys. Acta* **1808**, 2761–2771 (2011). Medline doi:10.1016/j.bbamem.2011.07.022

59. R. Mani, S. D. Cady, M. Tang, A. J. Waring, R. I. Lehrer, M. Hong, Membrane-dependent oligomeric structure and pore formation of a beta-hairpin antimicrobial peptide in lipid bilayers from solid-state NMR. *Proc. Natl. Acad. Sci. U.S.A.* **103**, 16242–16247 (2006). Medline doi:10.1073/pnas.0605079103

60. W. Luo, M. Hong, Determination of the oligomeric number and intermolecular distances of membrane protein assemblies by anisotropic 1H-driven spin diffusion NMR spectroscopy. *J. Am. Chem. Soc.* **128**, 7242–7251 (2006). Medline doi:10.1021/ja0603406

61. W. Luo, R. Mani, M. Hong, Sidechain conformation and gating of the M2 transmembrane peptide proton channel of influenza A virus from solid-state NMR. *J. Phys. Chem.* **111**, 10825–10832 (2007). doi:10.1021/jp073823k

62. K. Takegoshi, S. Nakamura, T. Terao, ^{13}C-^{1}H dipolar-assisted rotational resonance in magic-angle spinning NMR. *Chem. Phys. Lett.* **344**, 631–637 (2001). doi:10.1016/S0009-2614(01)00791-6

63. T. Gullion, J. Schaefer, Rotational echo double-resonance NMR. *J. Magn. Reson.* **81**, 196–200 (1989). Medline

64. M. G. Munowitz, R. G. Griffin, G. Bodenhausen, T. H. Huang, Two-dimensional rotational spin-echo NMR in solids: Correlation of chemical shift and dipolar interactions. *J. Am. Chem. Soc.* **103**, 2529–2533 (1981). doi:10.1021/ja00400a007

65. M. Hong, J. D. Gross, C. M. Rienstra, R. G. Griffin, K. K. Kumashiro, K. Schmidt-Rohr, Coupling amplification in 2D MAS NMR and its application to torsion angle determination in peptides. *J. Magn. Reson.* **129**, 85–92 (1997). Medline doi:10.1006/jmre.1997.1242

66. A. Bielecki, A. C. Kolbert, M. H. Levitt, Frequency-switched pulse sequences: Homonuclear decoupling and dilute spin NMR in solids. *Chem. Phys. Lett.* **155**, 341–346 (1989). doi:10.1016/0009-2614(89)87166-0

67. M. Hong, K. Schmidt-Rohr, Magic-angle-spinning NMR techniques for measuring long-range distances in biological macromolecules. *Acc. Chem. Res.* **46**, 2154–2163 (2013). Medline doi:10.1021/ar300294x